PRDM9 activity depends on HELLS and promotes local 5-hydroxymethylcytosine enrichment

Yukiko Imai[1]*[@], Mathilde Biot[1]*, Julie A. J. Clément[1], Mariko Teragaki[1], Serge Urbach[2], Thomas Robert[1#], Frédéric Baudat[1], Corinne Grey[1$] and Bernard de Massy[1$]

Affiliations

[1]: Institut de Génétique Humaine (IGH), Centre National de la Recherche Scientifique, Univ Montpellier, Montpellier, France

[2]: Institut de Génomique Fonctionnelle, Université de Montpellier, CNRS, INSERM, Montpellier, France.

@: Present address: Department of Gene Function and Phenomics, National Institute of Genetics, Mishima, Japan.

[#]: Present address: Centre de Biochimie Structurale (CBS), CNRS, INSERM, Univ Montpellier, Montpellier, France

*: equal contribution

[$]: corresponding authors

Keywords: meiosis/HELLS/LSH/5hmC/methylation/PRDM9/recombination

Abstract

Meiotic recombination starts with the formation of DNA double-strand breaks (DSBs) at specific genomic locations that correspond to PRDM9 binding sites. The molecular steps occurring from PRDM9 binding to DSB formation are unknown. Using proteomic approaches to find PRDM9 partners, we identified HELLS, a member of the SNF2-like family of chromatin remodelers. Upon functional analyses during mouse male meiosis, we demonstrated that HELLS is required for PRDM9 binding and DSB activity at PRDM9 sites. However, HELLS is not required for DSB activity at PRDM9-independent sites. HELLS is also essential for 5-hydroxymethylcytosine (5hmC) enrichment at PRDM9 sites. Analyses of 5hmC in mice deficient for SPO11, which catalyzes DSB formation, and in PRDM9 methyltransferase deficient mice reveal that 5hmC is triggered at DSB-prone sites upon PRDM9 binding and histone modification, but independent of DSB activity. These findings highlight the complex regulation of the chromatin and epigenetic environments at PRDM9-specified hotspots.

Introduction

In sexual reproduction, genetic information from both parental genomes is reassorted through chromosome segregation during meiosis. Additional genetic diversity is generated by recombination events between parental homologous chromosomes (homologs) that take place during the first meiotic prophase. Meiotic recombination leads to reciprocal (crossover) and non-reciprocal (gene conversion) transfer of genetic information. Crossovers establish physical links between homologs that are maintained until the end of prophase of the first meiotic division and are essential for the proper segregation of homologs at the first meiotic division. Gene conversion without crossovers promotes interactions between homologs, thus mechanistically contributing to the proper execution of the crossover pathway. Gene conversion also leads locally to the replacement of small regions (typically, from a few to a few hundred base pairs) from one parental genome to the other (J. M. Chen, Cooper, Chuzhanova, Ferec, & Patrinos, 2007). Therefore, meiotic homologous recombination enhances genetic diversity (Coop & Przeworski, 2007) and is essential for fertility (Hunter, 2015). Homologous recombination events are generated by the programmed induction of DNA double strand breaks (DSBs) followed by their repair, as a crossover or not, with a chromatid from the homolog (Baudat & de Massy, 2007). Meiotic DSBs are tightly controlled in time, space, and frequency in order to drive the homologous recombination pathway while keeping genome integrity (de Massy, 2013; Keeney, Lange, & Mohibullah, 2014; Sasaki, Lange, & Keeney, 2010).

Remarkably, two distinct pathways control DSB localization (Lichten & de Massy, 2011). In several species, including plants and fungi, DSBs occur at promoter regions or regions of accessible chromatin without detectable sequence specificity. This pattern of DSB localization has been thoroughly analyzed in *Saccharomyces cerevisiae* (Pan et al., 2011). The DSB machinery, which involves several proteins including Spo11 that carries the catalytic activity for DNA cleavage (de Massy, 2013), is somehow directed to such accessible chromatin sites. Several factors that act locally, such as chromatin structure, but also higher order chromosome organization features are important for DSB formation at these accessible regions (I. Lam & Keeney, 2014). In contrast, in humans and mice, and possibly in some non-mammalian species (Z. Baker et al., 2017), DSBs occur at sites bound by PRDM9 and not at promoters (Pratto et al., 2014; Smagulova et al., 2011). The *Prdm9* gene, which is

present in a wide range of metazoans, is expressed specifically in meiocytes, at the stage of meiotic DSB formation. It encodes a protein that has a sequence-specific DNA binding domain with multiple potential targets in the genome. PRDM9 also has a PR-SET domain with methyltransferase activity and promotes the tri-methylation of lysine 4 (H3K4me3) and of lysine 36 (H3K36me3) of histone H3 on nucleosomes adjacent to PRDM9 binding sites (Grey, Baudat, & de Massy, 2018). This methyltransferase activity is essential for DSB formation at PRDM9 sites (Diagouraga et al., 2018). In mice lacking PRDM9, DSBs form at promoters and enhancers (Brick, Smagulova, Khil, Camerini-Otero, & Petukhova, 2012; Mihola et al., 2019).

The various steps that take place from PRDM9 binding to DSB formation are still poorly understood. Specifically, it is not known how the DSB machinery is recruited or activated, and how the different molecular steps proceed in a local chromatin environment that is *a priori* not specified before PRDM9 binding. Moreover, upon binding, PRDM9 promotes chromatin modifications with the deposition of H3K4me3 and H3K36me3 on adjacent nucleosomes (C. L. Baker, Walker, Kajita, Petkov, & Paigen, 2014; Grey et al., 2017; Powers et al., 2016). One or both of these modifications are predicted to be required for DSB activity, because PRDM9 methyltransferase is essential for DSB activity at PRDM9 sites (Diagouraga et al., 2018), unless another substrate of PRDM9 methyltransferase is involved. In addition, these histone modifications may play a role in DSB repair. Indeed, ZCWPW1, a protein reader of H3K4me3 and H3K36me3, is required for efficient DSB repair (T. Huang et al., 2020; Li et al., 2019; Mahgoub et al., 2020; Wells et al., 2019). Whatever their exact role, the presence of both histone modifications leads to a unique chromatin landscape at PRDM9 sites that is not present at promoters, where H3K36me3 is depleted (Grey et al., 2017; K. G. Lam, Brick, Cheng, Pratto, & Camerini-Otero, 2019; Powers et al., 2016). Therefore, the specific chromatin environment at PRDM9 sites may be important for DSB activity and repair. In mice lacking PRDM9, where DSBs form mainly at promoters and enhancers, an inefficient DSB repair is observed (Brick et al., 2012; Hayashi & Matsui, 2006), which could be due to the chromatin environment at those sites, and/or alternatively to improper regulation of DSB formation.

Other histone modifications have been identified at PRDM9 sites (Buard, Barthes, Grey, & de Massy, 2009; Davies et al., 2016; K. G. Lam et al., 2019). It has been proposed that epigenetic features

at DSB hotspots are also responsible for some of the observed DSB activity differences in male and female mouse meiosis (Brick et al., 2018). Indeed, besides chromatin, the global cytosine methylation level is different between sexes: low in prophase oocytes (Kagiwada, Kurimoto, Hirota, Yamaji, & Saitou, 2013; Seisenberger et al., 2012) and high in spermatocytes (Gaysinskaya et al., 2018). Cytosine methylation is a dynamic epigenetic modification that can be removed by the actions of ten-eleven-translocation (TET) enzymes, the first product of which is 5-hydroxymethylcytosine (5hmC) (Tahiliani et al., 2009). Interestingly, a local increase in 5hmC has been detected at PRDM9 sites in mouse spermatocytes (Brick et al., 2018), indicative of another potential layer of modification at DSB sites.

To gain insights into these molecular steps and to identify proteins involved at PRDM9 binding sites, we developed a proteomic approach to identify PRDM9 partners. We found that HELLS, a member of the SNF2-like family of chromatin remodelers, interacts with PRDM9. This interaction has also been recently shown by Spruce and colleagues (Spruce et al., 2020). Interestingly, HELLS was previously implicated in the regulation of DNA methylation, transposable element expression, heterochromatin dynamics, and DSB repair in somatic cells (Burrage et al., 2012; Dennis, Fan, Geiman, Yan, & Muegge, 2001; Kollarovic, Topping, Shaw, & Chambers, 2020; Lungu, Muegge, Jeltsch, & Jurkowska, 2015; Yu, McIntosh, et al., 2014). HELLS is also required for female and male meiosis (De La Fuente et al., 2006; Zeng et al., 2011). A recent study showed that HELLS is needed for proper meiotic DSB localization and acts as a PRDM9-dependent chromatin remodeler of meiotic hotspots (Spruce et al., 2020). Here, we found that in mouse male meiosis, HELLS is directly involved in the control of DSB activity by ensuring PRDM9 binding and thus DSB formation at PRDM9-dependent sites, consistent with the results obtained by (Spruce et al., 2020). This HELLS activity appears to solve the challenge of chromatin accessibility for PRDM9 binding. We also show that HELLS-dependent PRDM9 binding and PRDM9 methyltransferase activity are required for efficient 5hmC enrichment at PRDM9 binding sites. This epigenetic modification is a feature of PRDM9-specified hotspots that is not dependent on DSB formation.

Results

HELLS interacts with PRDM9

To identify proteins that interact with PRDM9 we first chose to express a tagged version of human PRDM9 in HeLa S3 cells, which do not express PRDM9 (Morin et al., 2008), and performed immunoprecipitation (IP) followed by mass spectrometry analysis allowing us to identify candidates that are not germline specific. We generated two stable cell lines that express the human *PRDM9*^{A} allele (Baudat et al., 2010) with an epitope tag (FLAG-HA) inserted at the amino- (Nt) or carboxy-terminal (Ct) end (see Methods). Unmodified HeLa S3 cells were used as negative control. We purified tagged *PRDM9*^{A}-containing complexes from HeLa S3 cell nuclear extracts by FLAG affinity, followed by HA affinity purification (Table 1- source data File 1).

First, we carried out pilot experiments by selecting proteins with a size that ranged between 70 and 80 kD and between 95 and 120 kD after silver staining to potentially identify PRDM9 and other proteins, respectively. PRDM9 peptides were the first and the third most abundant peptides for Nt- and Ct-tagged PRDM9 respectively, only in the 70-80 kD size range (Table 1). Although the predicted molecular weight (MW) of tagged PRDM9 is 103 kD, its detection in the 70-80 kD size range is compatible with its faster than predicted migration during denaturing gel electrophoresis (see western blots in Table 1- source data File 1). HELLS peptides were the first and the second most abundant peptides for Nt- and Ct-tagged PRDM9, respectively, only in the 95-120 kD size range, in agreement with HELLS predicted MW (97 kD) (Jarvis et al., 1996). Then, we repeated the experiments, but without size selection and by analyzing the full protein content after affinity purification. This analysis confirmed the pilot experiment findings, and highlighted HELLS as a major PRDM9 partner. In this condition, with both Nt- and Ct-tagged PRDM9, HELLS was the first in the list of proteins identified by mass spectrometry and ranked by peptide abundance. We did not detect HELLS peptides in IP experiments from HeLa S3 cells without the PRDM9-expressing vector. The PRDM9 and HELLS peptide counts, and protein coverages are shown in Table 1 (see Supplementary File 1 for the full list

of proteins). We did not perform any other analysis or quantification of the proteome present in these samples for this study.

As HELLS is expressed in gonads and is essential for gametogenesis (De La Fuente et al., 2006; Zeng et al., 2011), we then tried but failed to detect any interaction between HELLS and PRDM9 by western blotting after IP of mouse testis protein extracts. This could be due to technical problems linked to the used antibodies since this interaction was recently detected in mouse testis extracts by (Spruce et al., 2020). Therefore, we used mass spectrometry after IP with a polyclonal antibody against PRDM9 or normal rabbit serum (mock) (Table 1, Table 1- source data File 1). The relative abundance of HELLS peptides was lower in the assays with mouse testis extracts compared with HeLa S3 cell extracts, partly due to higher noise. Nevertheless, HELLS peptides were enriched in extracts purified with the anti-PRDM9 antibody, compared with mock control. In three independent experiments, 14, 6, and 7 HELLS peptides were obtained after IP with the anti-PRDM9 antibody, and 6, 5, and 1 in the mock controls (Table 1). HELLS enrichment in IP experiments with the anti-PRDM9 antibody was also revealed by quantification based on the Label-Free-Quantification ranks (Table 1 and Supplementary File 1).

As a complementary approach to proteomics, we searched for PRDM9 partners by yeast two-hybrid screening. Using mouse PRDM9 without zinc fingers as bait and a mouse juvenile testis cDNA bank, we identified six clones that corresponded to HELLS, indicating a direct interaction between PRDM9 and HELLS. All six clones shared a domain that included residues 30 to 448 of HELLS (Figure 1). To better map the HELLS region involved in the interaction with PRDM9, we generated different HELLS constructs and found that the C-terminal region (569-821) of HELLS was dispensable for this interaction (Figure 1B). We could not detect any interaction with PRDM9 upon deletions at the N-terminus or C-terminus of the 1-569 region, such as in the HELLS constructs 193-569 and 1-408, respectively. This suggests the potential involvement of the N-terminal (1-193) and of the central (408-569) regions of HELLS in the interaction with PRDM9 (Figure 1B and Figure 1-figure supplement 1).

HELLS is required for PRDM9-dependent meiotic DSB formation

To evaluate the functional role of HELLS in meiotic recombination, we generated a mouse line in which *Hells* was conditionally ablated only during male meiosis by meiotic-specific expression of CRE under the control of the *Stra8* promoter on a transgene (Sadate-Ngatchou, Payne, Dearth, & Braun, 2008) (*Hells* cKO) (Figure 2- figure supplement 1), because HELLS is essential for mouse development (Geiman et al., 2001). A previous study where HELLS-deficient testes were analyzed by allografting embryonic tissues showed that HELLS is required for meiotic progression during spermatogenesis (Zeng et al., 2011). A potential interpretation for this meiotic defect was that alterations of DNA methylation in the absence of HELLS may affect, directly or indirectly, some properties of meiotic prophase and synapsis between homologous chromosomes (Zeng et al., 2011). This phenotype shares some similarity with the defects observed in *Hells* KO oocytes (defects in meiotic recombination and homologous synapsis, and changes in DNA methylation at repetitive DNA elements and pericentric heterochromatin) (De La Fuente et al., 2006).

Therefore, to test whether HELLS is directly implicated in meiotic recombination, we first precisely determined the meiotic stage(s) and steps that could be affected by HELLS depletion. In this study, we used various mouse strains with wild type *Hells* alleles (*Hells*$^{fl/+}$, *Hells*$^{fl/+}$ *Stra8-Cre*^{Tg}, *Hells*$^{fl/-}$) that are all named *Hells* CTRL hereafter. Meiotic-specific *Hells* mutant mice were *Hells*$^{fl/-}$ *Stra8-Cre*^{Tg} and are named *Hells* cKO hereafter.

Western blot analysis of wild type mouse testis whole cell extracts showed that HELLS protein could be detected from 4 days post-partum (dpp) to 15dpp and in adults. PRDM9 was detected from 9 dpp when cells have entered meiosis, but not at 4 and 6 dpp before meiosis entry (Figure 2-figure supplement 2). In testis nuclear extracts from 22dpp *Hells* cKO animals, HELLS level was greatly reduced (Figure 2A), but not the nuclear PRDM9 protein level. The residual HELLS protein expression in testis nuclear extracts from *Hells* cKO mice might be due to incomplete CRE-induced deletion of *Hells* in some spermatocytes, as suggested by the cytological analysis presented below. We analyzed HELLS staining by immunofluorescence on spread spermatocytes of adult *Hells* CTRL and *Hells* cKO mice (Figure 2B). In *Hells* CTRL nuclei, we could detect HELLS as punctuate staining that

covered nuclear chromatin, with the highest intensity at leptotene and zygotene and absence of specific staining at later stages (Figure 2- figure supplement 3). In *Hells* cKO nuclei, we did not detect HELLS staining in 75% of leptotene and zygotene nuclei, but could observe a weak HELLS staining in about 25% of nuclei (not shown). Thus, in some *Hells* cKO spermatocytes, HELLS expression was not completely abolished, and the protein was still present in the nucleus. Histological analysis of *Hells* cKO mice revealed spermatogenesis defects with 89% of tubules without haploid cells (Figure 2C, D), suggesting an arrest of spermatocyte differentiation. The presence of 11% of tubules with some haploid cells might be explained by incomplete HELLS depletion in some spermatocytes. Moreover, the percentage of tubules with one or more TUNEL-positive cells was increased, indicative of apoptotic cells undergoing massive genomic DNA breakage (Figure 2E and Figure 2- figure supplement 4).

By immunostaining of spread spermatocytes, we showed that in *Hells* cKO mice, spermatocytes entered meiotic prophase and progressed until a pachytene-like stage with chromosomes only partially synapsed in most nuclei, whereas some nuclei had fully synapsed chromosomes (Figure 2F), consistent with previous observations on *Hells*-deficient spermatocytes (Zeng et al., 2011). We detected chromosome axes by the presence of the axial protein SYCP3, and synapses by the presence of the central element protein SYCP1. Ninety three percent of *Hells* CTRL nuclei that showed full-length axes were at the pachytene stage with 19 fully synapsed autosomes and a γH2AFX-positive chromatin domain containing the X and Y-chromosomes, called sex body. In contrast, only 13% of *Hells* cKO nuclei with full-length axes were similar to wild-type looking pachytene nuclei. This population of wild type pachytene nuclei in *Hells* cKO mice could be due to incomplete depletion of HELLS in some spermatocytes, as discussed above.

Interestingly, in most *Hells* cKO spermatocytes, despite the normal level of nuclear PRDM9 detected by western blotting (Fig 2A), the PRDM9 signal detected by immunostaining was much reduced compared with wild type (Figure 2B, Figure 2- figure supplement 5). As in nuclear spreads proteins that are not tightly bound to chromatin can be partially lost, this low PRDM9 signal in *Hells* cKO samples could indicate that in the absence of HELLS, PRDM9 localizes in the nucleus, but does not bind to chromatin efficiently. Overall, the DSB activity did not seem to be affected because we

detected a large number of DMC1 foci. Conversely, DSB repair appeared to be defective, as indicated by the persistence of DMC1 and γH2AFX foci, and the absence of a normal XY sex body at the pachytene-like stage (Figure 2G).

To directly test DSB activity and localization in the absence of HELLS, we performed chromatin IP with an anti-DMC1 antibody followed by single-strand DNA sequencing (DMC1 ChIP-SSDS). DMC1 ChIP-SSDS allows recovering single-strand DNA bound by the strand exchange protein DMC1 (Khil, Smagulova, Brick, Camerini-Otero, & Petukhova, 2012). We performed these experiments in two wild type (*Hells* CTRL) and two *Hells* cKO mice. Both wild type and mutant mice express the PRDM9^{Dom2} variant that binds to a specific set of genomic sites and promotes DSB formation at those sites (Brick et al., 2012; Grey et al., 2017). We detected 11133 and 17117 peaks of DMC1 enrichment in the *Hells* CTRL and *Hells* cKO samples, respectively. This indicated the presence of DSB activity in both genetic contexts, as observed by immunofluorescence. However, only 1129 peaks were common, representing 10% of *Hells* CTRL peaks, and 6.6% of *Hells* cKO peaks (Figure 3A, Figure 3- figure supplement 1). Analysis of the signal intensity in the genotype-specific peaks (*Hells* CTRL -specific and *Hells* cKO-specific) showed the absence of detectable signal in one genotype within peaks specific to the other genotype (Figure 3B). In the 1129 common peaks, the average DMC1 enrichment intensity was higher in *Hells* CTRL than in *Hells* cKO samples (Figure 3B). Among these common peaks, analysis of individual peak intensities revealed three subgroups, one subgroup with stronger intensity in *Hells* CTRL (n=898 peaks), one subgroup with stronger intensity in *Hells* cKO (n=154 peaks), and a smaller subgroup (n=77 peaks) where the peak intensity was similar in both genotypes (Figure 3- figure supplement 2A). The group of 898 peaks with stronger intensity in *Hells* CTRL corresponded to DSB sites specified by PRDM9 ^{Dom2}. Indeed, an enrichment for H3K4me3 at these sites was observed specifically in the B6 strain that expresses PRDM9^{Dom2}, but not in the congenic RJ2 strain that expresses PRDM9^{Cst}, which binds to distinct genomic sites (Figure 3- figure supplement 2B). This suggests that these 898 peaks with stronger DMC1 intensity (in the cell population) in *Hells* CTRL may have a lower DSB level in *Hells* cKO, or may be active only in a smaller cell fraction in *Hells* cKO mice. We favor the second hypothesis, because our cytological analyses showed that HELLS is still detected in a small fraction of *Hells* cKO spermatocytes. The

group of 154 peaks with higher DMC1 enrichment in *Hells* cKO were in regions with PRDM9-independent H3K4me3 enrichment (Figure 3- figure supplement 2B), suggesting a specific induction of DSB activity at these sites in the absence of HELLS. The group of 77 peaks with similar DMC1 intensity in *Hells* CTRL and *Hells* cKO showed a weak PRDM9-independent H3K4me3 enrichment. A low level of DSB activity at PRDM9-independent sites has been detected in mice that express PRDM9, and could account for these peaks (Smagulova, Brick, Pu, Camerini-Otero, & Petukhova, 2016).

To better understand the low overlap of DMC1 peaks in *Hells* CTRL and *Hells* cKO mice, we compared the *Hells* cKO peaks with those mapped in *Prdm9* KO mice. When PRDM9 is defective (such as in *Prdm9* KO mice) DSBs are formed at a different set of genomic sites, also called default sites. These sites overlap mainly with promoters and enhancers and are enriched in H3K4me3 (Brick et al., 2012). Remarkably, 85% of *Hells* cKO peaks overlapped with peaks detected in *Prdm9* KO mice (Figure 3C, 3E). This demonstrated that in the absence of HELLS, DSBs are no longer formed at PRDM9 sites, but are induced at default sites, similarly to what observed in *Prdm9* KO mice (Figure 3E). The lower number of peaks detected in *Hells* cKO samples (17117) compared with *Prdm9* KO mice (27732) could be due to a lower signal in *Hells* cKO samples. We hypothesized that mainly low intensity peaks in *Prdm9* KO mice should be undetectable in *Hells* cKO mice, and mainly high intensity peaks in *Prdm9* KO should be detected in *Hells* cKO mice, thus contributing to the population of the 14543 overlapping peaks. Indeed, among the peaks mapped in *Prdm9* KO samples, the peaks that were identified as overlapping with *Hells* cKO peaks were biased toward higher intensity compared with non-overlapping peaks (Figure 3D). The lower signal detected in *Hells* cKO could be explained by a difference in the sensitivity of the current ChIP-SSDS experiment and/or by a difference in DSB activity.

PRDM9-dependent DSB sites are characterized by several features that are implemented independently of DSB formation: PRDM9 binding, and enrichment for H3K4me3, H3K36me3 and H3K9ac on adjacent nucleosomes (Buard et al., 2009; Davies et al., 2016; Grey et al., 2017; K. G. Lam et al., 2019; Powers et al., 2016; Spruce et al., 2020). To identify the step of PRDM9-dependent DSB site designation affected by the absence of HELLS, we tested by ChIP-qPCR, PRDM9 binding

and H3K4me3 levels at four representative PRDM9^{Dom2} binding sites (*Pbx1a*, *A3*, *14a*, *17b*) that were used as reference in previous studies (Billings et al., 2013; Diagouraga et al., 2018). Enrichment for PRDM9 and for H3K4me3 were strongly reduced (at least by four-fold) at all four sites in *Hells* cKO spermatocytes compared with *Hells* CTRL cells (Figure 3F). This indicates that HELLS is required for efficient PRDM9 binding to its sites, consistent with the strong reduction in PRDM9 signal detected by immunofluorescence (Figure 2B). Moreover, this result provides a molecular interpretation for the absence of DSB activity at PRDM9 binding sites in *Hells* cKO spermatocytes.

HELLS and PRDM9 are required for 5hmC enrichment at meiotic hotspots

Recently, it was shown that HELLS interacts with all three TET methylcytosine dioxygenases (de Dieuleveult et al., 2020; Jia et al., 2017). Upon oxidation, the activity of TET enzymes on methylated cytosines (5mC) leads to a first product, 5-hydroxymethylcytosine (5hmC). It has been proposed that 5mC conversion to 5hmC allows regulating 5mC levels for proper gene expression (reviewed in Williams, Christensen, & Helin, 2011). Unlike 5mC, 5hmC is globally associated with euchromatin and is depleted on heterochromatin in somatic cells (Ficz et al., 2011). Interestingly, in mouse male germ cells, 5hmC is enriched at some enhancers and promoters (Gan et al., 2013; Hammoud et al., 2014), and at meiotic DSB hotspots in pachytene spermatocytes (Brick et al., 2018).

To test whether 5hmC enrichment was correlated with the DNA binding specificity of PRDM9, we took advantage of two congenic mouse strains (B6 and RJ2) that express PRDM9 variants with distinct DNA binding specificities (PRDM9^{Dom2} and PRDM9^{Cst}, respectively). In both strains, the sites of PRDM9 binding and activity have been mapped, and localize to distinct sets of genomic sites (Grey et al., 2017). As the mapping of PRDM9-dependent DSB hotspots can be done with different molecular approaches (ChIP with anti-PRDM9, -H3K4me3, or -DMC1 antibodies), we used the DMC1 ChIP-SSDS data that provide the optimal specificity and sensitivity, as reference for hotspots (Grey et al., 2017). We performed the 5hmC analysis using genomic DNA isolated from 95% pure leptotene/zygotene cell populations (see Methods). In both B6 and RJ2 mouse strains, the 5hmC

signal was correlated with DMC1 enrichment (Figure 4A, 4B), demonstrating that 5hmC enrichment depends on PRDM9 binding to its genomic targets.

The heatmaps of 5hmC enrichment at DMC1 sites revealed a correlation between the strength of the DMC1 hotspots and that of 5hmC (Figure 4A). We obtained similar results when the heatmaps were generated based on sites defined by PRDM9 ChIP (Figure 4- figure supplement 1A). We also noted that the mean 5hmC signal at hotspots was higher in RJ2 than in B6 samples (Figure 4A, Figure 4- figure supplement 1A). This correlated with the greater occupancy of the $PRDM9^{Cst}$ variant (expressed in RJ2 mice) compared with the $PRDM9^{Dom2}$ variant (expressed in B6 mice) (Grey et al., 2017). The 5hmC enrichment analysis and specifically the average enrichment plots showed a narrow distribution of the 5hmC enrichment that extended about +/- 250bp from the peak center and overlapped closely with the enrichment profile of PRDM9 (Figure 4C). Peak centers were defined based on the DMC1 ChIP SSDS signal and have been previously shown to overlap with PRDM9 DNA binding motifs (Smagulova et al., 2011). However, 5hmC distribution was narrower than DMC1 distribution, which extends to the single-stranded DNA generated upon DSB end processing (Figure 4-figure supplement 1B). Moreover, the 5hmC maximum intensity was between the H3K4me3 peaks that delineate the positioned nucleosomes flanking the PRDM9 binding sites (C. L. Baker et al., 2014) (Figure 4- figure supplement 1B). Thus, 5hmC was predominantly taking place in the nucleosome-depleted region at and around PRDM9 binding sites.

Altogether, these findings suggest that 5hmC enrichment is functionally linked to PRDM9 binding activity. To directly test this hypothesis, we analyzed 5hmC in *Hells* cKO spermatocytes where PRDM9 binding to hotspots is defective (Figures 2B and 3F). Strikingly, 5hmC enrichment at hotspots was lost in *Hells* cKO spermatocytes (Figure 4D). This suggests that 5hmC enrichment at meiotic hotspots is promoted by HELLS and/or PRDM9 binding, or by one of the subsequent steps depending on HELLS and PRDM9. Therefore, we tested whether PRDM9 methyltransferase activity was required, using a mouse strain (named B6-Tg(YF)) where two PRDM9 variants of distinct DNA binding specificities are produced: the $PRDM9^{Dom2}$ variant with wild-type methyltransferase activity, and the $PRDM9^{Cst\text{-}YF}$ variant with defective methyltransferase activity due to a point mutation (Y357F)

in the SET domain (Diagouraga et al., 2018; Wu et al., 2013). Our previous study established that the PRDM9^{Cst-YF} variant binds to the binding sites of PRDM9^{Cst}, but cannot catalyze the methylation of the surrounding histones (Diagouraga et al., 2018). In B6-Tg(YF) mice, 5hmC was enriched at the B6 DMC1 sites (bound by PRDM9^{Dom2}), as expected, but not at the RJ2 DMC1 sites bound by PRDM9^{Cst-YF} (Figure 4E). We conclude that PRDM9 binding is not sufficient and that its methyltransferase activity is also required for 5hmC enrichment. Then, to test whether 5hmC enrichment required also DSB activity (or downstream events), we analyzed 5hmC enrichment at hotspots in *Spo11* KO mice in which DSB formation is defective. In these mice, 5hmC levels were identical to wild type mice (Figure 4F). This result indicates that DSB formation is not required for 5hmC, and that a step between PRDM9 histone modification and DSB formation leads to 5hmC enrichment at meiotic hotspots.

We then analyzed the correlation of 5hmC enrichment with the strength of PRDM9, H3K4me3, SPO11-oligos and DMC1 enrichment. SPO11-oligos are the molecular intermediates generated after DSB formation by endonucleolytic cleavage of the strand to which SPO11 is covalently bound (Neale, Pan, & Keeney, 2005). SPO11-oligos data are available only for the B6 genotype (Lange et al., 2016). DMC1 enrichment reflects DSB formation, but is also influenced by features of DSB repair, and is not directly proportional to SPO11-oligos (Hinch et al., 2019). The correlation plots revealed that in the RJ2 strain, 5hmC was best correlated with PRDM9 and H3K4me3 enrichment, and in the B6 strain, with SPO11-oligo enrichment (Figure 4-figure supplement 1C). In both strains, the weakest correlation was between 5hmC and DMC1. This suggests that 5hmC enrichment at hotspots is better correlated with events directly linked to PRDM9 binding and DSB activity, rather than to DSB repair, which is consistent with the functional dependency reported above.

As 5hmC level at hotspots may depend on the density of CpG dinucleotides and of 5mC, it was important to examine the same correlations in function of the CpG content within hotspots (Figure 5- figure supplement 1A). Over a +/- 250bp window around hotspot centers, the mean number of CpG was 4.4 (0.88 CpG/100b) in B6, and 4.3 (0.86 CpG/100b) in RJ2. Of note, the consensus motif for

PRDM9^{Dom2} and PRDM9^{Cst} does not include CpGs (C. L. Baker et al., 2015; Grey et al., 2017). The slight increase in CpG density around PRDM9^{Dom2} hotspot was expected due to the process of GC-biased gene conversion (Duret & Galtier, 2009) that leads to higher GC content at meiotic recombination hotspots (Clement & Arndt, 2013; Grey et al., 2017). We then examined the methylation level at CpGs within +/-250bp from B6 and RJ2 hotspot centers that contained at least one CpG using published sodium bisulfite data from B6 samples (Gaysinskaya et al., 2018). As control, we analyzed the methylation level at four different types of genomic sites: i) two families of transposable elements (LINE and IAP), and ii) two sets of imprinted control regions (ICRs): one set methylated only in females (female-specific) and the other methylated only in males (male-specific). As shown before (Ferguson-Smith, 2011), we observed low cytosine methylation levels at female-specific ICRs and high methylation levels at male-specific ICRs and the transposable elements LINE and IAP (Figure 5-figure supplement 1B). Meiotic hotspots specific for each strain (B6 and RJ2) showed a similar median methylation level of at least 90% at all stages analyzed (B type spermatogonia, leptotene and pachytene spermatocytes), with a level comparable to what observed in the genome (Figure 5-figure supplement 1B). Note that B6 hotspots, but not RJ2 hotspots, were active in the strain where methylation was monitored. This suggests that overall, in the cell population, the level of hotspot methylation is high already before they are bound by PRDM9, with no further detectable local increase of cytosine modification upon PRDM9 binding. This property was also mentioned in a recent study where the methylation level at DSB sites was measured by Nucleosome Occupancy and Methylome sequencing (NOMe-seq) at different stages during spermatogenesis (Y. Chen et al., 2020). As sodium bisulfite sequencing allows detecting both 5mC and 5hmC, we propose that the 5hmC enrichment we detected at active hotspots results from the conversion of pre-existing 5mC at these sites rather than *de novo* modification of unmodified cytosines.

We then evaluated the correlation between CpG content and 5hmC enrichment, by clustering hotspots according to their number of CpG dinucleotides within a region of +/-250bp around the center. We defined four groups of sites: i) no CpG, ii) 1-2 CpG, iii) 3-5 CpG, and iv) ≥ 6 CpG dinucleotides. The average plots revealed that sites with higher numbers of CpGs tended to have

higher 5hmC enrichment, in agreement with the fact that CpGs are the substrates for this modification (Figure 5A-5B, Figure 5-figure supplement 1C). In contrast, the number of CpGs was not correlated with hotspot activity. This is shown by the overlapping curves of average plots for the four groups of CpG content of PRDM9, H3K4me3 and DMC1 enrichment (Figure 5-figure supplement 1D). Heatmaps within each group of hotspots with similar numbers of CpGs revealed also that for a given CpG content, the 5hmC level correlated with the PRDM9, H3K4me3 and DMC1 site intensity (Figure 5 - figure supplement 1D), an observation coherent with the functional dependency on PRDM9 binding and methyltransferase activity reported above.

Discussion

A chromatin remodeler for PRDM9 binding

In 2010, the discovery that PRDM9 is the factor directing the location of meiotic DSBs in mammals raised several questions about the underlying molecular process. One of them was how the zinc finger domain of PRDM9 gains access to its DNA binding motifs. These DNA sites have no other reported function than being bound by PRDM9, and this occurs specifically in meiotic cells where *Prdm9* is expressed. These sites are located throughout the genome, in genic and intergenic regions, and they do not appear to have any intrinsic feature beyond their DNA sequence. The only identified landmark is their higher GC content relative to their flanking regions that appears progressively over generations due to the process of GC-biased gene conversion during meiotic DSB repair at these sites (Clement & Arndt, 2013; Grey et al., 2017). Moreover, PRDM9 binding sites can differ between mouse strains because the PRDM9 DNA binding domain is highly mutable, and multiple variants with distinct DNA binding specificity are present in *Mus musculus* (Buard et al., 2014; Kono et al., 2014; Vara et al., 2019).

One of the major advances of this study, together with the parallel study from C. Baker's group (Spruce et al., 2020), is the identification of the interaction between PRDM9 and HELLS, and

the evidence of its essential role in allowing PRDM9 to access and stably bind to its binding sites (Figure 5C). The interaction between PRDM9 and HELLS was detected by IP-mass spectrometry and by yeast two-hybrid assays (this study) and by co-IPs (Spruce et al., 2020). In addition, and consistent with these interactions, ChIP experiments showed that HELLS is enriched at least at a fraction of PRDM9 sites, presumably the ones with the most efficient PRDM9 binding (Spruce et al., 2020). The chromatin configuration of PRDM9 binding sites has been analyzed by accessibility to MNase and to the transposase Tn5 (ATAC-seq). Before PRDM9 expression (in spermatogonia), most PRDM9 binding sites do not reveal specific accessibility compared with flanking genomic sequences (Y. Chen et al., 2020). Conversely, when PRDM9 is expressed (leptonema), the binding sites show increased chromatin accessibility along few hundred base pairs on both sides of the PRDM9 binding site (C. L. Baker et al., 2014; Yamada et al., 2020). The footprint of PRDM9 binding is not detected by ATAC-seq, suggesting a short residency time (Spruce et al., 2020). As PRDM9 promotes H3K4me3 and H3K36me3 deposition on flanking nucleosomes, the chromatin organization at these sites can be examined and reveals a well-positioned arrangement of modified nucleosomes around PRDM9 binding sites. Overall, a striking change of chromatin configuration is observed upon PRDM9 binding, and HELLS plays an essential role in this process. This conclusion is based on the observation that in *Hells* cKO spermatocytes, PRDM9 binding (this study), PRDM9 dependent-H3K4me3 deposition, and chromatin accessibility (Spruce et al., 2020) cannot be detected at PRDM9 binding sites.

HELLS belongs to the SNF2-like family of chromatin remodelers (Flaus, Martin, Barton, & Owen-Hughes, 2006), but unlike other members of this family no ATP-dependent nucleosome remodeling activity could be detected *in vitro* (Burrage et al., 2012). However, in *Xenopus laevis* extracts, HELLS promotes nucleosome remodeling when forming a complex with CDCA7 that contains a 4-CXXC zinc finger domain (Jenness et al., 2018). Therefore, it could be anticipated that in meiotic cells, HELLS is brought to PRDM9 binding sites by interacting with PRDM9. HELLS-dependent steps, such as nucleosome repositioning and/or stabilization and the subsequent opening of chromatin, could further stabilize the interaction of the PRDM9 zinc finger domain with these sites, in a process partly similar to the one described for pioneer transcription factors (Mayran & Drouin, 2018). Functionally, HELLS absence leads to a phenotype comparable to the one observed upon

Prdm9 genetic ablation. Indeed, in *Hells* cKO mice, meiotic DSB activity is undetectable at PRDM9 sites and is redirected to sites of open chromatin, such as promoters and enhancers (this study; (Spruce et al., 2020)), which are called default sites, like in *Prdm9* KO mice (Brick et al., 2012). Therefore, HELLS is an essential determinant of meiotic DSB localization in mice.

Could HELLS have additional role(s) beyond promoting PRDM9 binding? As observed in *Prdm9* KO mice, *Hells* cKO mice show a partial defect in DSB repair and homologous synapsis. By promoting nucleosome reorganization at PRDM9 binding sites, HELLS may contribute to DNA repair. This contribution may concern the chromatin of the broken and also the uncut chromatid because it has been proposed that PRDM9 binds not only to the chromatid where DSBs will occur but also to the intact template (Davies et al., 2016; Hinch et al., 2019). Such "symmetric binding" might enhance interhomolog repair. In theory, HELLS activity could participate in DSB repair by regulating chromatin organization on the broken chromatid (for instance for strand resection), and on the uncut chromatid (for strand invasion). In support of this hypothesis, it has been shown that in somatic cells, HELLS is involved in and facilitates DSB repair (Burrage et al., 2012; Kollarovic et al., 2020). In somatic cells, HELLS might facilitate end-resection by interacting with and recruiting C-terminal interacting protein (CtIP) (Kollarovic et al., 2020). HELLS implication in genome integrity has also been detected in *Neurospora crassa* (Basenko, Kamei, Ji, Schmitz, & Lewis, 2016) and *Saccharomyces cerevisiae* (Litwin, Bakowski, Maciaszczyk-Dziubinska, & Wysocki, 2017). In *S. cerevisiae*, the HELLS orthologue Irc5 is required for DNA damage tolerance, and this function implies the loading of the cohesin complex at replication forks (Litwin et al., 2018). In *S. cerevisiae*, cohesin recruitment facilitates DSB repair (Strom, Lindroos, Shirahige, & Sjogren, 2004; Unal et al., 2004). The hypothesis of a role for HELLS in meiotic DSB repair through enhancing end-resection and/or cohesin loading remains to be tested.

In other cellular contexts, HELLS is a major regulator of DNA methylation, specifically for the silencing of repeated DNA elements, and through the recruitment of the DNA methyltransferase DNMT3B (Myant & Stancheva, 2008; Zhu et al., 2006). This has an impact on DNA methylation genome-wide (Ren, Finney, Ni, Cam, & Muegge, 2019; Yu, Briones, et al., 2014). Besides altering epigenetic features and the expression of transposable elements (TE), HELLS absence in mouse

tissues (brain and liver) and in fibroblasts has very limited consequences on gene expression (J. Huang et al., 2004; Yu, McIntosh, et al., 2014). In *Hells* KO mouse oocytes, the DNA methylation level of some TE families is reduced and their expression is increased; however, the expression of several meiotic genes is not affected (De La Fuente et al., 2006). The consequences of *Hells* deficiency on DNA methylation and expression have not been tested in spermatocytes. However, in the absence of HELLS, major epigenomic alterations in non-repeated DNA are not expected during meiosis, and consistently, H3K4me3 level at promoters is not altered in *Hells* cKO spermatocytes (Spruce et al., 2020).

The implication of 5-hydroxymethylcytosine at meiotic DSB sites

The presence of 5hmC at DSB hotspots was first reported by Brick and colleagues (Brick et al., 2018) using genome-wide data on cytosine methylation and hydroxyl-methylation patterns in mouse spermatocytes, mainly at the pachytene stage (Hammoud et al., 2014). Here, we found that this DNA modification is also present at hotpots earlier in meiosis, at leptotene-zygotene stages, when DSB formation takes place. By assessing 5hmC in mouse strains that carry different *Prdm9* alleles (*Prdm9*^{Dom2} and *Prdm9*^{Cst}), we found that 5hmC deposition depends on PRDM9 DNA binding specificity. Moreover, we detected 5hmC enrichment in a narrow window of about +/-250 bp around the center of PRDM9 binding sites. Remarkably, PRDM9 binding is not sufficient and PRDM9 methyltransferase activity also is required for 5hmC enrichment. As we showed that 5hmC presence at hotspots does not require SPO11, we propose that 5hmC is promoted by a PRDM9-dependent chromatin modification step before DSB formation (Figure 5C). Therefore, 5hmC is a new feature of the local signature of active hotspots, like the histone modifications H3K4me3, H3K4me36 and H3K9ac (Buard et al., 2009; Davies et al., 2016; Grey et al., 2017; K. G. Lam et al., 2019; Powers et al., 2016).

The next question concerns the mechanism of the 5hmC enrichment at PRDM9-dependent hotspots. This enrichment is not observed in somatic tissues (Brick et al., 2018), which is consistent with the PRDM9 dependency we observed and with the PRDM9-specific expression at the leptotene

stage of the meiotic prophase (Jung et al., 2019; Spruce et al., 2020). In the mouse male germline, a high level of DNA methylation is induced genome-wide during germline development in spermatogonia before meiosis entry and is maintained during meiotic prophase with a transient reduction at preleptonema (Gaysinskaya et al., 2018). A similar high DNA methylation level is observed at meiotic DSB sites (Figure 5 - figure supplement 1D; (Y. Chen et al., 2020)). Therefore, it could be hypothesized that a TET enzyme promoting the conversion of 5mC to 5hmC (Ito et al., 2010) is recruited upon or concomitantly with PRDM9 binding to its sites. One possible scenario could be that TET recruitment involves HELLS. Indeed, HELLS can interact with one, two, or all three TET enzymes, depending on the cell type (MCF-7 cells, Hek293T, mouse embryonic stem cells) (de Dieuleveult et al., 2020; Jia et al., 2017), and co-localize with 5hmC when stably expressed in HK1 cells (Jia et al., 2017). As no evidence of HELLS/TET interaction in meiotic cells is available, a PRDM9-dependent chromatin modification might be implicated in recruiting the putative TET activity. ZCWPW1, a reader of H3K4me3 and H3K36me3 that is required for efficient DSB repair (T. Huang et al., 2020; Mahgoub et al., 2020; Wells et al., 2019), might be directly or indirectly involved in this recruitment.

The function of 5hmC at meiotic hotspots is unknown. At least two non-exclusive consequences of 5hmC can be envisioned. First, as 5hmC has been associated with sites of open chromatin, such as active and poised enhancers, in several cell types (Serandour et al., 2012; Stroud, Greenberg, Feng, Bernatavichute, & Jacobsen, 2013; Szulwach et al., 2011), it could have an active role in recruiting partners or stabilizing interactions, similarly to the recruitment of factors described in neuronal progenitor cells (Spruijt et al., 2013). Second, it has been shown that 5hmC prevents the binding of several methyl-CpG-binding proteins (Jin, Kadam, & Pfeifer, 2010). One or both of these consequences of the conversion of 5mC to 5hmC could have a positive effect on DSB repair at meiotic hotspots in male meiosis. We favor the second scenario, in which the conversion of 5mC to 5hmC allows antagonizing the binding of factors with affinity for 5mC and which could interfere with meiotic recombination. Indeed, it is difficult to reconcile a positive role for 5hmC with the observation that DSB formation and repair is efficient at hotspots without CpGs in spermatocytes, and at all hotspots in oocytes, which have a low global level of cytosine methylation (Seisenberger et al., 2012).

The control of initiation sites of meiotic recombination by PRDM9 underlies a sophisticated regulation that goes beyond the simple binding to specific DNA motifs in the genome. Clearly, our findings and those from Baker's laboratory (Spruce et al., 2020) indicate that the control of chromatin is an important step for DSB formation and repair. PRDM9 and HELLS drive epigenetic modifications before and independently of DSB formation, setting the stage for downstream steps. Not only histone modifications but also DNA methylation appears to be a potential additional level of regulation of meiotic recombination, with potential distinct consequences during male and female meiosis where some differences in hotspot activity have been detected (Brick et al., 2018) and from the analysis of 5hmC in the male germ line presented in this study. These observations also highlight the need of understanding the sex-specific features of meiotic recombination in general.

Methods

Key resources table

Reagent type (species) or resource	Designation	Source or reference	Identifiers	Additional information
Mouse strains				
	C57BL/6JOlaHsd	Envigo	C57BL/6JOlaHsd	Named B6
	B10.MOLSGR(A)-(D17Mit58-D17Jcs11)/Bdm (RJ2)	Grey et al., 2009	MGI:5319075	Named RJ2
	B6;129P2 <Prdm9tm1Ymat>/J	Hayashi et al., 2005	MGI:3624989	Named *Prdm9* KO
	Spo11<tm1Mjn>	Baudat et al., 2000	MGI:2178805	Named *Spo11* KO
	Hells<tm1a(EUCOMM)Wtsi/Ieg>	EUCOM Bradley et al., 2012	MGI:4431905	
	C57BL/6 Tg(CAG-Flpo)1Afst	Kranz et al., 2010	MGI:4453967	
	C57BL/6 Tg(CMV-cre)1Cgn	Schwenk et al., 1995	MGI:2176180	
	Tg(Stra8-icre)1Reb/J <(Stra8-iCre)>	Sadate-Ngatchou et al., 2008	MGI:3779079	
	Tg(RP23-159N6*)23Bdm	Diagoura ga et al., 2018	MGI:5565212	Named B6-Tg(YF)
Cell lines				
	HeLa	ATCC	HeLa S3 ATCC® CCL-2.2	
Yeast strains				
	AH109	James et al., 1996		*S. cerevisiae*
	Y187	Harper et al., 1993		*S. cerevisiae*
Recombinant DNA reagents				
	PRDM9A-Flag-HA-Nt into retroviral pOZ-FH-N vector	This study	N/A	Vector from Addgene DB3781
	PRDM9A-Flag-HA-Ct into retroviral pOZ-FH-C vector	This study	N/A	Vector from Addgene cat# 32516
	pGAD GH for fusion to Gal4 activation domain, modified for Gateway cloning	Van Aelst., 1993	Clontech No. 638853	LEU2 marker
	pAS2dd for fusion to Gal4 DNA binding domain, modified for Gateway cloning	Fromont-Racine et al., 1997		TRP1 marker
	pB29 for PRDM9 (aa 1-511) expression fused to LexA for yeast two hybrid screen	Hybrigeni cs		

Antibodies				
	Guinea-pig anti-SYCP3	Grey et al. 2009	N/A	Home-made WB: 1/2000 IF: 1/500
	Rabbit anti-SYCP1	Abcam	Cat# ab15090 RRID: AB_301636	IF: 1/400
	Rabbit anti-DMC1	Santa Cruz	Cat# scH100 RRID: AB_2277191	IF: 1/200
	Goat anti-DMC1	Santa Cruz	Cat# scC20 RRID: AB_2091206	ChIP: 24µg
	Rabbit anti-HELLS	Novus	Cat# NB 100-278 RRID: AB_350198	WB: 1/2000 IF: 1/200
	Mouse monoclonal anti-HELLS	Santa Cruz	Cat# sc46665 RRID: AB_627895	IF: 1/100
	Mouse monoclonal anti-phospho-histone H2AFX (Ser139)	Millipore	Cat# MP05-636 RRID: AB_309864	Named γH2AFX IF: 1/10000
	Rabbit anti-Gal4 activation domain (GAD) (Millipore, 06-283)		Now at Sigma-Aldrich Cat# ABE476	WB: 1/3000
	Rabbit anti-Gal4 DNA-Binding domain	Sigma Aldrich	Cat# G3042 RRID: RRID:AB_439688	WB: 1/2000
	Rat monoclonal anti-Tubulin [YOL1/34]	Abcam	Cat# ab 6161 RRID: RRID:AB_305329	WB: 1/3000
	Rabbit anti-5hmC	Active Motif	Cat# AM 39791 RRID: AB_2630381	hMeDIP: 5µg
	Rabbit anti-PRDM9	Grey et al. 2017	N/A	Home-made WB: 1/2000 IF: 1/200 ChIP: 4µg
	Rabbit anti-H3K4me3	Abcam	ab8580 RRID: AB_306649	ChIP: 4µg
	Goat anti-rabbit IgG-HRP	Pierce	Cat# 1858415 RRID:AB_1185567	WB: 1/10000
	Goat anti-guinea pig IgG-HRP	Jackson Immuno Research	Cat# 706-035-148 RRID: AB_2340447	WB: 1/3000
	Goat anti-rabbit IgG-Alexa 555	Thermo Fisher Scientific	Cat# ab150078 RRID: AB_2535849	IF: 1/400
	Goat anti-guinea pig IgG-Alexa 488	Thermo Fisher Scientific	Cat# ab150185 RRID: AB_2534117	IF: 1/400
	Donkey anti-mouse IgG-Alexa 680	Thermo Fisher Scientific	Cat# ab175774 RRID: AB_2534014	IF: 1/100
	Donkey anti-mouse IgG-Alexa 647	Thermo Fisher Scientific	Cat# ab150107 RRID: AB_162542	IF: 1/400
Oligonucleotides				
	Genotyping *Hells* cKO mice, see Supplementary file 2	This study		
	RT-qPCR, see Supplementary file 3	This study, Buard et al. 2009, Diagoura	N/A	

		ga et al. 2018		
Commercial assays or kits				
	DeadEnd Fluorometric TUNEL System	Promega	Cat# G3250	
	Anti-HA beads	Santa Cruz	Cat# sc-500773	
	EZview anti-FLAG M2 Affinity Gel	Sigma Aldrich	Cat# F2426	
	hMeDIP Kit	Actif Motif	Cat# AM55010	
	NEB Next Ultra Library Preparation Kit	New England Biolabs	Cat# NEB7370S	
	ChIP-IT High Sensitivity Kit	Actif Motif	Cat# AM53040	
	MMLV-based retroviral transduction system	Nakatani et al. 2003	N/A	
Chemical compounds				
	HA peptide	Covance	Cat #PEP-101P-1000	
	FLAG peptide	Sigma	Cat #F4799	
	Optiprep Idoixanol	Sigma Aldrich	Cat# D1556	
	Sytox Green	Thermo Fisher Scientific	Cat# S70020	
	WIN 18466	Tocris Bioscience	Cat# 4736	Hogarth et al. 2013
	Retinoic Acid	Sigma Aldrich	Cat# R2625	
Deposited data				
	Mass spectrometry proteomics	ProteomeXchange Consortium	Dataset identifier PXD017337	
	NGS SSDS ChIP (DMC1) and hMeDIP	GEO	GSE145768	
Softwares and Algorithms				
	Bowtie 2		http://bowtie-bio.sourceforge.net/bowtie2/index.shtml	
	Modified BWA algorithm	Khil et al. 2012	N/A	
	Tim Galore!		https://www.bioinformatics.babraham.ac.uk/projects/trim_galore/	
	Bismark		https://www.bioinformatics.babraham.ac.uk/projects/bismark/	
	Bedtools suite		https://bedtools.readthedocs.io/en/latest/content/bedtools-suite.html	

536

537

Mouse strains

The following mouse strains were used: C57BL/6JOlaHsd (hereafter B6), B10.MOLSGR(A)-(D17Mit58-D17Jcs11)/Bdm (RJ2)(Grey, Baudat, & de Massy, 2009), B6;129P2-*Prdm9*^{tm1Ymat}/J (B6 PRDM9^{KO}) (Hayashi, Yoshida, & Matsui, 2005), *Spo11*^{tm1Mjn} (B6 SPO11^{KO}) (Baudat, Manova, Yuen, Jasin, & Keeney, 2000), C57BL/6J-Tg(RP23-159N6*)23Bdm (B6-Tg(YF)) (Diagouraga et al., 2018). *Hells*$^{tm1a(EUCOMM)Wtsi/Ieg}$ mice (EUCOM consortium (Bradley et al., 2012)) have a C57BL/6N genetic background with the *Prdm9*^{Dom2} allele. These mice were mated with mice expressing FLP from the CMV promoter (C57BL/6 Tg(CAG-Flpo)1Afst) (Kranz et al., 2010) to generate a floxed (*Hells*^{fl}) allele. *Hells*$^{fl/fl}$ mice were mated with mice that express CRE under the control of the CMV promoter (C57BL/6 Tg(CMV-cre)1Cgn) (Schwenk, Baron, & Rajewsky, 1995) to generate *Hells*-deleted heterozygous mice (*Hells*$^{+/-}$). *Hells*$^{+/-}$ mice were mated with Tg(Stra8-icre)1Reb/J (*Stra8-Cre*^{Tg}) mice (Sadate-Ngatchou et al., 2008) to generate *Hells*$^{+/-}$;*Stra8-Cre*^{Tg} mice. By crossing *Hells*$^{fl/fl}$ mice with *Hells*$^{+/-}$;*Stra8-Cre*^{Tg} mice, *Hells*$^{fl/-}$;*Stra8-Cre*^{Tg} (*Hells* cKO) mice and *Hells*$^{fl/+}$, *Hells*$^{fl/+}$ *Stra8-Cre*^{Tg} or *Hells*$^{fl/-}$ (*Hells* CTRL) mice were obtained. RJ2 mice have a C57BL/10 genetic background, very similar to that of B6, and carry the *Prdm9*^{Cst} allele. B6-Tg(YF) mice carry both the endogenous wild-type *Prdm9*^{Dom2} allele and the transgenic methyltransferase-dead *Prdm9*$^{Cst\text{-}YF}$ allele (Y357F mutation on *Prdm9*^{Cst} allele) on a BAC transgene. All experiments were carried out according to the CNRS guidelines and were approved by the ethics committee on live animals (project CE-LR-0812 and 1295).

HeLa cells

Generation of HeLa cells that express human PRDM9^{A} tagged with Flag-HA

To generate HeLa S3 cells that express PRDM9 tagged with Flag and HA, the previously described MMLV-based retroviral transduction system was used (Nakatani & Ogryzko, 2003). Human PRDM9^{A} was cloned in the pOZ-FH-N and pOZ-FH-C derivative vectors to express PRDM9^{A}-Flag-HA-Nt and PRDM9^{A}-Flag-HA-Ct, respectively. The HeLa S3 cell lines expressing PRDM9^{A}-Flag-HA-Nt and PRDM9^{A}-Flag-HA-Ct were generated.

Preparation of HeLa cell protein extracts

Nuclear protein extracts were prepared from 1 L (~10^8 cells) of cell culture using the Dignam protocol (Dignam, Martin, Shastry, & Roeder, 1983) with minor modifications. Extracts were prepared from cells that express PRDM9^A-Flag-HA-Nt, PRDM9^A-Flag-HA-Ct or without expression vector.

Immunoprecipitation of HeLa cell protein extracts

The PRDM9 complex was purified by immunoprecipitation (IP) using anti-FLAG (IP-FLAG) and -HA antibodies (IP-HA). About 35 mg of proteins from each nuclear fraction were used. FLAG affinity purification was performed with EZview anti-FLAG M2 Affinity Gel (Sigma). Elution was performed with 0.2 mg/ml of FLAG peptide. HA affinity purification was performed with anti-HA beads (Santa Cruz). Elution was performed with 0.4 mg/ml HA peptide (eluate 1 and 2) and 2 mg/ml HA peptide (eluate 3). Eluates 1 and 2 were analyzed on 4-15% acrylamide gels by silver staining (Silver Quest™ Staining Kit, Invitrogen).

Mass spectrometry of HeLa cell immunoprecipitates

Eluates 1 and 2 of IP-HA were pooled and analyzed by mass spectrometry. The pooled proteins were precipitated with the TCA method using the ProteoExtract® Protein Precipitation Kit (Calbiochem). All samples purified from protein extracts of PRDM9-Nt- and -Ct-expressing, or non-PRDM9-expressing HeLa cells were analyzed using a Velos-Orbitrap Pro mass spectrometer (Thermo Scientific) at the Taplin Mass Spectrometry Facility. The mass spectrometry data were analyzed with GFY, an application developed in Gygi's laboratory (Harvard University). Pilot experiments were performed with size separation by gel electrophoresis and protein extraction from slices corresponding to the MW of 70-80 kD and of 95-120 kD before mass spectrometry (130927, samples 43346 to 43351). For the full proteomic analysis, whole samples were sequenced (131026, samples 43738 to 43740). The list of proteins is in Supplementary File 1. Proteins defined as contaminants according to the Crapome and Mitocheck databases (www.crapome.org and www.mitocheck.org/) were removed.

Preparation of mouse testis protein extracts

For mass spectrometry experiments, nuclear extracts were prepared from mouse testes from 12-13 dpp C57BL/6 mice (n=18). Proteins were extracted from nuclei following the Dignam protocol (Dignam, Lebovitz, & Roeder, 1983).

For analysis of PRDM9 and HELLS expression during mouse spermatogenesis, whole cell extracts were prepared from frozen testes collected from 4, 6, 9, 12, 15 dpp, and adult RJ2 males. Extraction was performed by homogenizing cells with a Dounce homogenizer in 400mM NaCl, 50mM Hepes, 1% Triton X-100, 4mM DTT, complete protease inhibitor, followed by sonication and centrifugation to remove debris.

For PRDM9 and HELLS expression analysis in testes from 22 dpp *Hells* CTRL and *Hells* cKO mice, nuclear extracts were prepared. Testes were homogenized in hypotonic buffer (10 mM Hepes, pH 8.0, 320 mM sucrose, 1 mM PMSF, 1x Complete protease inhibitor cocktail EDTA-free (Roche, Cat. Number 11873580001)) in a Dounce homogenizer. After centrifugation (1,000xg at 4°C for 10min), supernatants were collected and used as cytoplasmic fractions. Nuclear fractions were from pellets that were resuspended in RIPA buffer (50 mM Tris–HCl, pH 7.5, 150 mM NaCl, 1 mM EDTA, 1% NP-40, 0.5% Na-deoxycholate, 0.1% SDS, 1x Complete protease inhibitor EDTA-free (Roche)), sonicated and centrifuged to remove debris.

Western blotting

For PRDM9 and HELLS expression analysis in testes from 22 dpp *Hells* CTRL and *Hells* cKO mice, nuclear fractions (40 µg) were analyzed by western blotting with affinity-purified rabbit anti-PRDM9 (1/2,000) (Grey et al., 2017) and rabbit anti-HELLS (NB100-278, Novus) (1/2,000) antibodies and guinea pig serum raised against the mouse SYCP3 residues 24-44 (1/2,000). Secondary antibodies were goat anti-rabbit IgG-HRP (1/10,000) (1858415, Pierce) and goat anti-guinea pig IgG-HRP (1/3,000) (706-035-148, Jackson Immuno Research).

For PRDM9 and HELLS expression during mouse spermatogenesis, 50µg of whole cell extracts were analyzed by western blotting with affinity-purified rabbit anti-PRDM9 (Grey et al., 2017), mouse anti-HELLS (SC-46665, Santa-Cruz) and rat anti-tubulin (ab6161, Abcam) antibodies.

Immunoprecipitation of mouse testis nuclear protein extracts

IP-PRDM9 and IP-Control (mock) were performed with 4µg of anti-PRDM9 antibody (Grey et al., 2017) or normal rabbit serum and 3.6-3.8 mg of nuclear proteins after pre-clearing with protein A or G Dynabeads (Invitrogen).

Mass spectrometry of mouse testis protein samples

IP samples were analyzed after separation on 7.5% acrylamide gels and silver staining (Silver QuestTM Staining Kit, Invitrogen). Protein extraction and purification were monitored by western blotting with an anti-PRDM9 antibody (Grey et al., 2017). IP samples were analyzed on an LTQ Velos Pro Orbitrap Elite mass spectrometer (Thermo Scientific), and the obtained data were processed with the MaxQuant software at the Functional Proteomics Platform (IGF, Montpellier). The data outputs include the intensity-based absolute quantification (iBAQ) and label-free quantification (LFQ) intensities for each protein. The iBAQ value is the sum of the intensities of all tryptic peptides for each protein. Therefore, iBAQ values are proportional to the protein molar quantities. LFQ intensities are based on the intensities of each protein and are normalized at multiple levels to ensure that the LFQ intensity profiles across samples accurately reflect the protein relative amounts. Raw data are available at Proteome Exchange. Samples are: 150310_MS_ver3, Res_PRMD9_150805 (two duplicates). The protein list with the quantifications is in Supplementary File 1. Data have been deposited in ProteomeXchange, reference PXD017337.

Yeast two-hybrid assays

All plasmids used in yeast two-hybrid assays were cloned with the Gateway® Gene Cloning Technology (Invitrogen) and transformed in the AH109 and Y187 haploid strains. These strains were

transformed with Gal4 DNA binding domain (GBD) and Gal4 activation domain (GAD) fusion plasmids, respectively. Purified colonies of diploid strains were streaked on SD media plates lacking leucine and tryptophan (LW), or leucine, tryptophan and histidine (LWH), or leucine, tryptophan and histidine with 5mM amino-triazole (LWH+5mMAT). Interactions between GAD- and GBD-fusion proteins were evaluated after cell growth at 30°C for 3 days. For verification of protein expression, protein extracts were prepared and analyzed by western blotting, as previously described (Imai et al., 2017). The yeast two-hybrid screen was performed by Hybrigenics using a mouse cDNA library prepared using RNA from testes of 14-16 dpp mice.

Antibodies

Guinea pig anti-SYCP3 (Grey et al., 2009), rabbit anti-SYCP1 (Abcam, 15090), rabbit anti-DMC1 (Santa Cruz, H100), rabbit anti-HELLS (Novus, NB100-278), mouse monoclonal anti-HELLS (Santa Cruz, sc46665), and mouse monoclonal anti-phospho-histone H2AFX (Ser139) antibody (γH2AFX) (Millipore, 05-636) were used for immunostaining. For IP, a home-made anti-PRDM9 antibody was used (Grey et al., 2017). For western blots, anti-PRDM9 (Grey et al., 2017), anti-HELLS (Novus, NB100-278), anti-SYCP3 (Grey et al., 2009), anti-GAD (Millipore, 06-283), anti-GBD (Sigma, G3042), and anti-tubulin (Abcam, ab6161) antibodies were used. For 5hmC analysis, a rabbit anti-5hmC antibody (Active Motif, 39791) was used. For DMC1 ChIP-SSDS, a goat anti-DMC1 antibody (Santa Cruz, C-20) was used. For conventional ChIP experiments, rabbit anti-PRDM9 (Grey et al., 2017) and rabbit anti-H3K4me3 (Abcam, ab8580) antibodies were used.

Histological analysis of paraffin sections and TUNEL assay

Mouse testes were fixed in Bouin's solution for Periodic Acid Schiff (PAS) staining, or in 4% paraformaldehyde/1X PBS for immunostaining or TUNEL assay, at room temperature overnight. Testes were then embedded in paraffin and cut in 3µm-thick slices. PAS-stained sections were scanned using the automated tissue slide-scanning tool of a Hamamatsu NanoZoomer Digital

Pathology system. TUNEL assay was performed with the DeadEnd Fluorometric TUNEL System (Promega), according to the manufacturer's protocol.

Immunostaining of nuclei spreads and fixed nuclei

Characterization of *Hells* cKO spermatocytes and meiotic staging of spermatocytes after synchronization were performed on nuclei spreads. Meiotic staging after Fluorescence-Activated Cell Sorting (FACS) was performed using fixed nuclei deposited on poly-lysine coated slides. Spreads were prepared with the dry down technique, as described (Peters, Plug, van Vugt, & de Boer, 1997), and immunostaining was performed as described (Grey et al., 2009). Staging criteria were the following: pre-leptotene nuclei had weak SYCP3 nuclear signal and no or very weak γH2AFX signal; leptotene nuclei were γH2AFX-positive and SYCP1-negative; early/mid zygotene nuclei had less than nine fully synapsed chromosomes; late zygotene had nine or more fully synapsed chromosomes; and pachytene cells had all chromosomes fully synapsed, excepted for the sex chromosomes. The following antibodies were used: rabbit anti-PRDM9 (Grey et al., 2017), 1:200), rabbit anti-HELLS (NB100-278, Novus, 1:200), mouse anti-HELLS (sc46665, Santa Cruz, 1:100), rabbit anti-DMC1 (H-100, Santa Cruz, 1:200), guinea-pig anti-SYCP3 ((Grey et al., 2009), 1:500), anti-SYCP1 (ab15090, Abcam, 1:400) and anti-γH2AFX (05-636, Millipore, 1:10,000).

Synchronization of meiosis in male mice

The first wave of spermatogonia entry into meiosis initiates at 8 days postpartum (8dpp). Then, spermatocytes progress to meiotic prophase and reach the leptotene, zygotene and pachytene stages at approximately 11, 13 and 15dpp, respectively. Hence, the proportion of cells at leptotene/zygotene is 55%, 41% and 26% at these three ages, respectively (Goetz, Chandley, & Speed, 1984). To obtain a more enriched proportion of leptotene/zygotene spermatocytes, germ cell development was synchronized *in vivo* by manipulating the retinoic acid metabolism, as described in (Romer, de Rooij, Kojima, & Page, 2018). Briefly, at day 2 post-partum, mice were treated daily (by pipette feeding) with WIN 18,446 (100µg/gram of body weight), an inhibitor of retinoic acid synthesis that blocks the differentiation of spermatogonia and thus meiosis entry (Hogarth et al., 2013). After 8 to 10 days of

treatment, meiosis was initiated synchronously by a single intraperitoneal injection of 100µg of retinoic acid in 10µL of DMSO. Between 8 and 9 days after the injection, mice were sacrificed and testes were harvested. At this time point, about 80-85% of spermatocytes were at leptotene/zygotene stage, as assessed by SYCP3, SYCP1 and γH2AFX staining on spermatocyte spreads performed using a small proportion of testis tissue. The remaining testis tissue was processed for nuclei purification and FACS sorting.

Purification of spermatocyte nuclei and FACS sorting

Synchronized decapsulated testes were fixed in 1% formaldehyde for 10 min. After quenching the reaction, tissues were homogenized and cells were lysed by homogenization with a tight fit homogenizer in homogenizing buffer (50mM sucrose, 25mMKCl, 5mM $MgCl_2$, 50mM NH_4Cl, 120mM tris pH7.4). After centrifugation, cells were resuspended in iodixanol-based Optiprep density gradient solution (Sigma-Aldrich D1556). First, a 50% iodixanol working solution was prepared by diluting the Optiprep density gradient solution in working solution (150mM KCl, 30mM MgCl2, 120mM Tris pH 7.4) at a ration 1:5. Then, the 50% iodixanol working solution was diluted to a final concentration of 27% in diluent solution (250mM sucrose, 25mM KCl, 5mM MgCl2, 20mM Tris pH7.4). Resuspended cells were centrifuged at 10,000g at 4°C for 30 min. After discarding the supernatants, isolated nuclei were labeled in labeling solution (1x Sytox green (Thermo Fisher Scientific, S70020) in 250mM sucrose, 25mM KCl, 5mM $MgCl_2$, 20mM tris pH7.4, 1% BSA) at room temperature for 2 hours. Labeled nuclei were filtered through a 70µm cell strainer and FACS-sorted with a BD FACS Melody sorter (100µm sort nozzle, 2,000-4,000 events/sec, 34 kHz). First, single nuclei were gated based on their light scatter (forward and reverse side scatter) properties. Second, 4C nuclei were gated based on their DNA content assessed through the fluorescence emitted by the Sytox green fixed on DNA observed with the 488 nm laser. Third, 4C nuclei were separated based on light scatter to gate leptotene-zygotene nuclei. Then, about 10 000 sorted nuclei were deposited on each poly-lysine-coated slide and immunostained with anti-SYCP3, -γH2AFX and -SYCP1 antibodies to verify the prophase I stage. Staining conditions and dilutions are the same as described above. Only

samples containing ≥90% of nuclei in leptotene and zygotene stage were used for experiments (see below).

Immunoprecipitation of genomic DNA containing 5-hydroxymethylcytosine (hMeDIP)

hMeDIP was performed using 5µg of genomic DNA extracted from a population of 1.5 to 2 $*10^6$ leptotene/zygotene spermatocytes (95% pure) (see above). Genomic DNA was obtained by phenol/chloroform extraction and then sonicated to a size of ~150bp with a Bioruptor pico apparatus (Diagenode, B01060010). Then, Illumina adaptors were added using the NEB Next Ultra Library Preparation Kit (NEB7370S), without the final PCR step. Finally, hMeDIP was performed with the Active Motif hMeDIP Kit (AM, 55010), according to the manufacturers' manual. Enriched fragments were then amplified by PCR using 12 cycles, as recommended by the NEB Next Ultra Library Preparation Kit. Sequencing was performed on a HiSeqX (2x150bp).

Chromatin immunoprecipitation of PRDM9 and H3K4me3

ChIP experiments were performed with the ChIP-IT High Sensitivity Kit (Active-motif, 53040). Briefly, testes from two or three synchronized mice (see above) were de-capsulated and fixed in complete tissue fixation solution for 10 min. After quenching the reaction, tissues were homogenized, and cell suspensions prepared by filtering samples through a 40µm cell strainer. Cells were washed twice with ice-cold 1x PBS, and chromatin was extracted and immunoprecipitated according to the manufacturers' instructions. 30-40 µg of chromatin was used per IP. The following antibodies (amount) were used: affinity purified anti-PRDM9 (4µg), anti-H3K4me3 (4µg).

Quantitative PCR

Immunoprecipitated DNA was quantified using real-time PCR, as described in (Buard et al., 2009). The immunoprecipitated fraction at all Dom2-specific hotspots (ChIP/Input ratio) was normalized to the immunoprecipitated fraction at the Cast-specific hotspot Hlx1.6, where no PRDM9 or H3K4me3 enrichment is detected in B6 mice that express $PRDM9^{Dom2}$ (Diagouraga et al., 2018). As a control for

the sample and IP quality, H3K4me3 level was measured at the *Sycp1* promoter. The primer sequences and PCR conditions for the studied sequence tagged sites (STS) (*Pbx1a, 14a, A3, 17b, Hlx1.6, Psmb9.8* and *Sycp1* promoter) were described previously (Buard et al., 2009) and are listed in Supplementary File 3.

DMC1 ChIP-SSDS

DMC1 ChIP-SSDS and library preparation were performed as described in (Grey et al., 2017). Two testes from 5-week-old *Hells*$^{fl/-}$ (named *Hells* CTRL in the main text) and three testes from 9-week-old *Hells* cKO mice were used for each replicate. Sequencing was performed on an HiSeq 2500 Rapidmode apparatus (2x150b).

Next generation sequencing data computational analysis

Read alignment

After quality control, 5hMeDIP-seq and DMC1 ChIP-SSDS reads were trimmed to 50bp and filtered to keep the sequencing read quality Phred score >28. Reads were then mapped to the UCSC mouse genome assembly build GRCm38/mm10. Mapping was done with Bowtie 2 (version 2.3.2) for the 5hMeDIP-seq experiment, using the single-end mode. DMC1 ChIP-SSDS reads were mapped using the previously published tools (Khil et al., 2012) that allow dealing with the specificities of this experiment. Only non-duplicated and uniquely mapped reads were kept after all alignments and used for the subsequent analysis.

Identifying meiotic hotspots using DMC1 ChIP-SSDS data

To identify meiotic hotspots from biologically replicated samples analyzed by DMC1 ChIP-SSDS, the Irreproducible Discovery Rate (IDR) methodology was used, as previously described for this experiment (Diagouraga et al., 2018). This method was developed for ChIP-seq analysis and extensively used in the ENCODE and modENCODE projects (Landt et al., 2012). The framework

777 developed by Qunhua Li and Peter Bickel's group
778 (https://sites.google.com/site/anshulkundaje/projects/idr) was followed. Briefly, this method allows
779 testing the reproducibility within and between replicates by using the IDR statistics. Following their
780 pipeline, peak calling was performed using MACS version 2.0.10 with relaxed conditions (--
781 pvalue=0.1 --bw1000 --nomodel --shift400) for each of the two replicates, the pooled dataset, and
782 pseudo-replicates that were artificially generated by randomly sampling half of the reads twice for
783 each replicate and the pooled dataset. Then IDR analyses were performed, and reproducibility was
784 checked. Final peak sets were built by selecting the top N peaks from pooled datasets (ranked by
785 increasing p values), with N defined as the highest value between N1 (the number of overlapping
786 peaks with an IDR <0.01, when comparing pseudo-replicates from pooled datasets) and N2 (the
787 number of overlapping peaks with an IDR <0.05 when comparing the true replicates), as
788 recommended for the mouse genome. Reproducibility between DMC1 replicates was double-checked
789 by testing their peak strength correlation calculated on the peaks recovered after IDR (Pearson's
790 correlation coefficients were: 0.99 and 0.96 for *Hells* CTRL and *Hells* cKO; Figure 3- figure
791 supplement 1).

792 ***Comparisons of DSB hotspot maps***

793 All DSB hotspot maps were compared by identifying overlapping (and non-overlapping) peak centers
794 ±200bp. First, it was confirmed that the control (i.e. *Hells* CTRL mice) DSB map reflected the wild-
795 type situation, with 96% of *Hells* CTRL DSB hotspots overlapping with the DSB map in B6 mice
796 (Grey et al., 2017), and up to 99% when compared with another DSB map in B6 mice (Smagulova et
797 al., 2016). Then, the *Hells* CTRL and *Hells* cKO and the *Hells* cKO and *Prdm9* KO DSB maps were
798 compared (Figure 3A and 3C). DSB hotspots and signals were also visually inspected along the
799 genome (a representative view around position 185Mb of chromosome 1 is shown in Figure 3E).

800 ***Signal normalization and quantitative analysis (DMC1, 5hmC and 5mC)***

801 If not otherwise stated, all read distributions and signal intensities presented in this work were
802 calculated after pooling reads from both replicates and were expressed as read per millions of mapped

reads or fragments. DMC1 ChIP-SSDS signal at DSB hotspots was calculated after peak re-centering, and fragment count was normalized to the local background, as previously described (Brick et al., 2012), then normalized to the library size (estimated as the sum of type1-ssDNA, type2-ssDNA and dsDNA). As we previously stated (Papanikos et al., 2019), normalization between *Hells* CTRL and *Hells* cKO samples could not be computed because of altered DMC1 dynamics in the *Hells* cKO. The 5hMeDIP-seq signal was calculated at different genomic regions (the region type and size are detailed in the figure legends) by subtracting the library-normalized input signal from the library-normalized 5hMeDIP-seq signal. For Figure 5 and Figure 5-figure supplement 1C and D, DMC1-SSDS B6 or RJ2 sites were divided in four groups, containing an increasing number of CpGs (0, 1-2, 3-5, and ≥6) within a window of +/-250bp around the peak center. Besides the group without CpGs, groups were defined in order to have similar numbers of DMC1-SSDS sites, as follows: 0 CpGs (812 and 821 for the B6 and RJ2 strains respectively); 1-2 CpGs (3915 and 4126 for the B6 and RJ2 strains, respectively); 3-5 CpGs (5649 and 5851 for the B6 and RJ2 strains, respectively); ≥6 CpGs (4384 and 4377 for the B6 and RJ2 strains, respectively). The 5mC signal at whole genome scale, at DSB sites, in LINE, IAPs and ICRs was calculated from whole-genome bisulfite sequencing data from (Gaysinskaya et al., 2018). (PRJNA326117). After removing adapter contamination and low-quality reads using trim galore, bisulfite-converted reads were mapped to the UCSC mouse genome assembly build GRCm38/mm10. Mapping in a paired-end mode and methylation call was done using Bismark. Duplicates were not discarded. For the subsequent analysis, only regions with at least one CpG and one informative read were considered. Using the Bedtools suite, the DNA methylation ratio was averaged in 1kb sliding, non-overlapping windows at the whole genome scale and in the whole interval at DSB sites, in LINE, IAP and ICRs. Median values of 5mC were higher than those reported by Gaysinskaya et al. (2018) and by Y. Chen et al. (2020). For instance, at leptonema, we obtained a genome-wide median DNA methylation level of 91% compared to 77 and 81% respectively in these two studies. These differences, which do not alter the conclusions could be due to the procedures used for reads selection and/or quantification.

Statistical analysis

The statistical analysis of cytological observations was done with GrapPad Prism 7. Statistical tests for DMC1 ChIP SSDS were done using R version 3.6.0, and for hMeDIP with python 3.7.4. All tests and p-values are provided in the corresponding legends and/or figures.

Data

The mass spectrometry proteomics data were deposited in ProteomeXchange Consortium via the PRIDE [1] partner repository with the dataset identifier PXD017337.

Reviewer account details:

Username: reviewer86230@ebi.ac.uk

Password: mHSXnRSX

NGS data have been deposited at GEO under series record GSE145768

Acknowledgments

We thank the following BioCampus Montpellier facilities for providing excellent technical support: the Réseau des Animaleries de Montpellier (RAM) for animal care, the Réseau d'Histologie Expérimentale de Montpellier (RHEM) for histology, and Montpellier Resources Imagerie (MRI) for microscopy, with help from Amélie Sarrazin for FACS. Mass spectrometry experiments were carried out using facilities of the Functional Proteomics Platform of Montpellier. We thank Rhea Kang and Francesca Cole for great teaching and training of M.B to the spermatogenesis synchronization protocol. We thank Christophe Grunau and the epigenomic platform (http://ihpe.univ-perp.fr/plateforme-epigenetique) for alignments of sequencing data of bisulfite-treated samples and Jihan Basbous for help in HeLa cells verification. This platform is supported with the support of LabEx CeMEB, an ANR "Investissements d'avenir" program (ANR-10-LABX-04-01). We thank Dan O' Carroll for sending us mice that harbor the Stra8-iCre transgene. We thank Yuki Shinya for performing several yeast two-hybrid assays, Lucile Marion-Poll for advices for FACS on fixed

purified nuclei, and James Hutchins for advices on mass spectrometry analysis. BdM was funded by grants from the Centre National pour la Recherche Scientifique (CNRS), the European Research Council (ERC) Executive Agency under the European Community's Seventh Framework Programme (FP7/2007-2013 Grant Agreement no. [322788]) and MSDAVENIR. BdM was recipient of the Prize Coups d'Élan for French Research from the Fondation Bettencourt-Schueller. MB was funded by a PhD fellowship from Fondation pour la recherche médicale (FRM).

Materials and correspondence.

To be addressed to:

Bernard de Massy: bernard.de-massy@igh.cnrs.fr

Corinne Grey: corinne.grey@igh.cnrs.fr

References

Baker, C. L., Kajita, S., Walker, M., Saxl, R. L., Raghupathy, N., Choi, K., . . . Paigen, K. (2015). PRDM9 Drives Evolutionary Erosion of Hotspots in Mus musculus through Haplotype-Specific Initiation of Meiotic Recombination. *PLoS Genet, 11*(1), e1004916. doi:10.1371/journal.pgen.1004916

Baker, C. L., Walker, M., Kajita, S., Petkov, P. M., & Paigen, K. (2014). PRDM9 binding organizes hotspot nucleosomes and limits Holliday junction migration. *Genome Res, 24*(5), 724-732. doi:10.1101/gr.170167.113

Baker, Z., Schumer, M., Haba, Y., Bashkirova, L., Holland, C., Rosenthal, G. G., & Przeworski, M. (2017). Repeated losses of PRDM9-directed recombination despite the conservation of PRDM9 across vertebrates. *elife, 6*. doi:10.7554/eLife.24133

Basenko, E. Y., Kamei, M., Ji, L., Schmitz, R. J., & Lewis, Z. A. (2016). The LSH/DDM1 Homolog MUS-30 Is Required for Genome Stability, but Not for DNA Methylation in Neurospora crassa. *PLoS Genet, 12*(1), e1005790. doi:10.1371/journal.pgen.1005790

Baudat, F., Buard, J., Grey, C., Fledel-Alon, A., Ober, C., Przeworski, M., . . . de Massy, B. (2010). PRDM9 is a major determinant of meiotic recombination hotspots in humans and mice. *Science, 327*(5967), 836-840. doi:science.1183439 [pii]10.1126/science.1183439

Baudat, F., & de Massy, B. (2007). Regulating double-stranded DNA break repair towards crossover or non-crossover during mammalian meiosis. *Chromosome Res, 15*(5), 565-577.

Baudat, F., Manova, K., Yuen, J. P., Jasin, M., & Keeney, S. (2000). Chromosome synapsis defects and sexually dimorphic meiotic progression in mice lacking spo11. *Mol Cell, 6*(5), 989-998.

Billings, T., Parvanov, E. D., Baker, C. L., Walker, M., Paigen, K., & Petkov, P. M. (2013). DNA binding specificities of the long zinc finger recombination protein PRDM9. *Genome Biol, 14*(4), R35. doi:10.1186/gb-2013-14-4-r35

Bradley, A., Anastassiadis, K., Ayadi, A., Battey, J. F., Bell, C., Birling, M. C., . . . Wurst, W. (2012). The mammalian gene function resource: the International Knockout Mouse Consortium. *Mamm Genome, 23*(9-10), 580-586. doi:10.1007/s00335-012-9422-2

Brick, K., Smagulova, F., Khil, P., Camerini-Otero, R. D., & Petukhova, G. V. (2012). Genetic recombination is directed away from functional genomic elements in mice. *Nature, 485*(7400), 642-645. doi:10.1038/nature11089

Brick, K., Thibault-Sennett, S., Smagulova, F., Lam, K. G., Pu, Y., Pratto, F., . . . Petukhova, G. V. (2018). Extensive sex differences at the initiation of genetic recombination. *Nature, 561*(7723), 338-342. doi:10.1038/s41586-018-0492-5

Buard, J., Barthes, P., Grey, C., & de Massy, B. (2009). Distinct histone modifications define initiation and repair of meiotic recombination in the mouse. *EMBO J, 28*(17), 2616-2624. doi:emboj2009207 [pii]10.1038/emboj.2009.207

Buard, J., Rivals, E., Dunoyer de Segonzac, D., Garres, C., Caminade, P., de Massy, B., & Boursot, P. (2014). Diversity of Prdm9 Zinc Finger Array in Wild Mice Unravels New Facets of the Evolutionary Turnover of this Coding Minisatellite. *PLoS One, 9*(1), e85021. doi:10.1371/journal.pone.0085021

Burrage, J., Termanis, A., Geissner, A., Myant, K., Gordon, K., & Stancheva, I. (2012). The SNF2 family ATPase LSH promotes phosphorylation of H2AX and efficient repair of DNA double-strand breaks in mammalian cells. *J Cell Sci, 125*(Pt 22), 5524-5534. doi:10.1242/jcs.111252

Chen, J. M., Cooper, D. N., Chuzhanova, N., Ferec, C., & Patrinos, G. P. (2007). Gene conversion: mechanisms, evolution and human disease. *Nat Rev Genet, 8*(10), 762-775. doi:nrg2193 [pii]10.1038/nrg2193

Chen, Y., Lyu, R., Rong, B., Zheng, Y., Lin, Z., Dai, R., . . . Tong, M. H. (2020). Refined spatial temporal epigenomic profiling reveals intrinsic connection between PRDM9-mediated H3K4me3 and the fate of double-stranded breaks. *Cell Res*. doi:10.1038/s41422-020-0281-1

Clement, Y., & Arndt, P. F. (2013). Meiotic recombination strongly influences GC-content evolution in short regions in the mouse genome. *Mol Biol Evol, 30*(12), 2612-2618. doi:10.1093/molbev/mst154

Coop, G., & Przeworski, M. (2007). An evolutionary view of human recombination. *Nat Rev Genet, 8*(1), 23-34.

Davies, B., Hatton, E., Altemose, N., Hussin, J. G., Pratto, F., Zhang, G., . . . Donnelly, P. (2016). Re-engineering the zinc fingers of PRDM9 reverses hybrid sterility in mice. *Nature, 530*(7589), 171-176. doi:10.1038/nature16931

de Dieuleveult, M., Bizet, M., Colin, L., Calonne, E., Bachman, M., Li, C., . . . Deplus, R. (2020). The chromatin remodeler LSH controls genome-wide cytosine hydroxymethylation. *Biorxiv*.

De La Fuente, R., Baumann, C., Fan, T., Schmidtmann, A., Dobrinski, I., & Muegge, K. (2006). Lsh is required for meiotic chromosome synapsis and retrotransposon silencing in female germ cells. *Nat Cell Biol, 8*(12), 1448-1454. doi:10.1038/ncb1513

de Massy, B. (2013). Initiation of meiotic recombination: how and where? Conservation and specificities among eukaryotes. *Annu Rev Genet, 47*, 563-599. doi:10.1146/annurev-genet-110711-155423

Dennis, K., Fan, T., Geiman, T., Yan, Q., & Muegge, K. (2001). Lsh, a member of the SNF2 family, is required for genome-wide methylation. *Genes Dev, 15*(22), 2940-2944. doi:10.1101/gad.929101

Diagouraga, B., Clement, J. A. J., Duret, L., Kadlec, J., de Massy, B., & Baudat, F. (2018). PRDM9 Methyltransferase Activity Is Essential for Meiotic DNA Double-Strand Break Formation at Its Binding Sites. *Mol Cell, 69*(5), 853-865 e856. doi:10.1016/j.molcel.2018.01.033

Dignam, J. D., Lebovitz, R. M., & Roeder, R. G. (1983). Accurate transcription initiation by RNA polymerase II in a soluble extract from isolated mammalian nuclei. *Nucleic Acids Res, 11*(5), 1475-1489. Retrieved from http://www.ncbi.nlm.nih.gov/pubmed/6828386

Dignam, J. D., Martin, P. L., Shastry, B. S., & Roeder, R. G. (1983). Eukaryotic gene transcription with purified components. *Methods Enzymol, 101*, 582-598. Retrieved from http://www.ncbi.nlm.nih.gov/pubmed/6888276

945 Duret, L., & Galtier, N. (2009). Biased gene conversion and the evolution of mammalian genomic
946 landscapes. *Annu Rev Genomics Hum Genet, 10*, 285-311. doi:10.1146/annurev-genom-
947 082908-150001
948 Ferguson-Smith, A. C. (2011). Genomic imprinting: the emergence of an epigenetic paradigm. *Nat*
949 *Rev Genet, 12*(8), 565-575. doi:10.1038/nrg3032
950 Ficz, G., Branco, M. R., Seisenberger, S., Santos, F., Krueger, F., Hore, T. A., . . . Reik, W. (2011).
951 Dynamic regulation of 5-hydroxymethylcytosine in mouse ES cells and during differentiation.
952 *Nature, 473*(7347), 398-402. doi:10.1038/nature10008
953 Flaus, A., Martin, D. M., Barton, G. J., & Owen-Hughes, T. (2006). Identification of multiple distinct
954 Snf2 subfamilies with conserved structural motifs. *Nucleic Acids Res, 34*(10), 2887-2905.
955 doi:10.1093/nar/gkl295
956 Fromont-Racine, M., Rain, J. C., & Legrain, P. (1997). Toward a functional analysis of the yeast
957 genome through exhaustive two-hybrid screens. Nat Genet, 16(3), 277-282.
958 doi:10.1038/ng0797-277
959 Gan, H., Wen, L., Liao, S., Lin, X., Ma, T., Liu, J., . . . Tang, F. (2013). Dynamics of 5-
960 hydroxymethylcytosine during mouse spermatogenesis. *Nat Commun, 4*, 1995.
961 doi:10.1038/ncomms2995
962 Gaysinskaya, V., Miller, B. F., De Luca, C., van der Heijden, G. W., Hansen, K. D., & Bortvin, A. (2018).
963 Transient reduction of DNA methylation at the onset of meiosis in male mice. *Epigenetics*
964 *Chromatin, 11*(1), 15. doi:10.1186/s13072-018-0186-0
965 Geiman, T. M., Tessarollo, L., Anver, M. R., Kopp, J. B., Ward, J. M., & Muegge, K. (2001). Lsh, a SNF2
966 family member, is required for normal murine development. *Biochim Biophys Acta, 1526*(2),
967 211-220. doi:10.1016/s0304-4165(01)00129-5
968 Goetz, P., Chandley, A. C., & Speed, R. M. (1984). Morphological and temporal sequence of meiotic
969 prophase development at puberty in the male mouse. *Journal of Cell Science, 65*, 249-263.
970 Grey, C., Baudat, F., & de Massy, B. (2009). Genome-Wide Control of the Distribution of Meiotic
971 Recombination. *PLoS Biol, 7*(2), e35. doi:08-PLBI-RA-2767 [pii]10.1371/journal.pbio.1000035
972 [doi]
973 Grey, C., Baudat, F., & de Massy, B. (2018). PRDM9, a driver of the genetic map. *PLoS Genet, 14*(8),
974 e1007479. doi:10.1371/journal.pgen.1007479
975 Grey, C., Clement, J. A., Buard, J., Leblanc, B., Gut, I., Gut, M., . . . de Massy, B. (2017). In vivo binding
976 of PRDM9 reveals interactions with noncanonical genomic sites. *Genome Res, 27*(4), 580-590.
977 doi:10.1101/gr.217240.116
978 Hammoud, S. S., Low, D. H., Yi, C., Carrell, D. T., Guccione, E., & Cairns, B. R. (2014). Chromatin and
979 transcription transitions of mammalian adult germline stem cells and spermatogenesis. *Cell*
980 *Stem Cell, 15*(2), 239-253. doi:10.1016/j.stem.2014.04.006
981 Harper, J. W., Adami, G. R., Wei, N., Keyomarsi, K., & Elledge, S. J. (1993). The p21 Cdk-interacting
982 protein Cip1 is a potent inhibitor of G1 cyclin-dependent kinases. Cell, 75(4), 805-816.
983 doi:10.1016/0092-8674(93)90499-g
984 Hayashi, K., & Matsui, Y. (2006). Meisetz, a novel histone tri-methyltransferase, regulates meiosis-
985 specific epigenesis. *Cell Cycle, 5*(6), 615-620.
986 Hayashi, K., Yoshida, K., & Matsui, Y. (2005). A histone H3 methyltransferase controls epigenetic
987 events required for meiotic prophase. *Nature, 438*(7066), 374-378.
988 Hinch, A. G., Zhang, G., Becker, P. W., Moralli, D., Hinch, R., Davies, B., . . . Donnelly, P. (2019). Factors
989 influencing meiotic recombination revealed by whole-genome sequencing of single sperm.
990 *Science, 363*(6433). doi:10.1126/science.aau8861
991 Hogarth, C. A., Evanoff, R., Mitchell, D., Kent, T., Small, C., Amory, J. K., & Griswold, M. D. (2013).
992 Turning a spermatogenic wave into a tsunami: synchronizing murine spermatogenesis using
993 WIN 18,446. *Biol Reprod, 88*(2), 40. doi:10.1095/biolreprod.112.105346

Huang, J., Fan, T., Yan, Q., Zhu, H., Fox, S., Issaq, H. J., . . . Muegge, K. (2004). Lsh, an epigenetic guardian of repetitive elements. *Nucleic Acids Res, 32*(17), 5019-5028. doi:10.1093/nar/gkh821

Huang, T., Yuan, S., Gao, L., Li, M., Yu, X., Zhang, J., . . . Liu, H. (2020). The histone modification reader ZCWPW1 links histone methylation to PRDM9-induced double strand break repair. *elife, 9*. doi:10.7554/eLife.53459

Hunter, N. (2015). Meiotic Recombination: The Essence of Heredity. *Cold Spring Harb Perspect Biol, 7*(12). doi:10.1101/cshperspect.a016618

Imai, Y., Baudat, F., Taillepierre, M., Stanzione, M., Toth, A., & de Massy, B. (2017). The PRDM9 KRAB domain is required for meiosis and involved in protein interactions. *Chromosoma, 126*(6), 681-695. doi:10.1007/s00412-017-0631-z

Ito, S., D'Alessio, A. C., Taranova, O. V., Hong, K., Sowers, L. C., & Zhang, Y. (2010). Role of Tet proteins in 5mC to 5hmC conversion, ES-cell self-renewal and inner cell mass specification. *Nature, 466*(7310), 1129-1133. doi:10.1038/nature09303

James, P., Halladay, J., & Craig, E. A. (1996). Genomic libraries and a host strain designed for highly efficient two-hybrid selection in yeast. Genetics, 144(4), 1425-1436. Retrieved from https://www.ncbi.nlm.nih.gov/pubmed/8978031

Jarvis, C. D., Geiman, T., Vila-Storm, M. P., Osipovich, O., Akella, U., Candeias, S., . . . Muegge, K. (1996). A novel putative helicase produced in early murine lymphocytes. *Gene, 169*(2), 203-207. doi:10.1016/0378-1119(95)00843-8

Jenness, C., Giunta, S., Muller, M. M., Kimura, H., Muir, T. W., & Funabiki, H. (2018). HELLS and CDCA7 comprise a bipartite nucleosome remodeling complex defective in ICF syndrome. *Proc Natl Acad Sci U S A, 115*(5), E876-E885. doi:10.1073/pnas.1717509115

Jia, J., Shi, Y., Chen, L., Lai, W., Yan, B., Jiang, Y., . . . Tao, Y. (2017). Decrease in Lymphoid Specific Helicase and 5-hydroxymethylcytosine Is Associated with Metastasis and Genome Instability. *Theranostics, 7*(16), 3920-3932. doi:10.7150/thno.21389

Jin, S. G., Kadam, S., & Pfeifer, G. P. (2010). Examination of the specificity of DNA methylation profiling techniques towards 5-methylcytosine and 5-hydroxymethylcytosine. *Nucleic Acids Res, 38*(11), e125. doi:10.1093/nar/gkq223

Jung, M., Wells, D., Rusch, J., Ahmad, S., Marchini, J., Myers, S. R., & Conrad, D. F. (2019). Unified single-cell analysis of testis gene regulation and pathology in five mouse strains. *elife, 8*. doi:10.7554/eLife.43966

Kagiwada, S., Kurimoto, K., Hirota, T., Yamaji, M., & Saitou, M. (2013). Replication-coupled passive DNA demethylation for the erasure of genome imprints in mice. *EMBO J, 32*(3), 340-353. doi:10.1038/emboj.2012.331

Keeney, S., Lange, J., & Mohibullah, N. (2014). Self-organization of meiotic recombination initiation: general principles and molecular pathways. *Annu Rev Genet, 48*, 187-214. doi:10.1146/annurev-genet-120213-092304

Khil, P. P., Smagulova, F., Brick, K. M., Camerini-Otero, R. D., & Petukhova, G. V. (2012). Sensitive mapping of recombination hotspots using sequencing-based detection of ssDNA. *Genome Res, 22*(5), 957-965. doi:10.1101/gr.130583.111

Kollarovic, G., Topping, C. E., Shaw, E. P., & Chambers, A. L. (2020). The human HELLS chromatin remodelling protein promotes end resection to facilitate homologous recombination and contributes to DSB repair within heterochromatin. *Nucleic Acids Res, 48*(4), 1872-1885. doi:10.1093/nar/gkz1146

Kono, H., Tamura, M., Osada, N., Suzuki, H., Abe, K., Moriwaki, K., . . . Shiroishi, T. (2014). Prdm9 polymorphism unveils mouse evolutionary tracks. *DNA Res, 21*(3), 315-326. doi:10.1093/dnares/dst059

Kranz, A., Fu, J., Duerschke, K., Weidlich, S., Naumann, R., Stewart, A. F., & Anastassiadis, K. (2010). An improved Flp deleter mouse in C57Bl/6 based on Flpo recombinase. *Genesis, 48*(8), 512-520. doi:10.1002/dvg.20641

Lam, I., & Keeney, S. (2014). Mechanism and regulation of meiotic recombination initiation. *Cold Spring Harb Perspect Biol, 7*(1), a016634. doi:10.1101/cshperspect.a016634

Lam, K. G., Brick, K., Cheng, G., Pratto, F., & Camerini-Otero, R. D. (2019). Cell-type-specific genomics reveals histone modification dynamics in mammalian meiosis. *Nat Commun, 10*(1), 3821. doi:10.1038/s41467-019-11820-7

Landt, S. G., Marinov, G. K., Kundaje, A., Kheradpour, P., Pauli, F., Batzoglou, S., . . . Snyder, M. (2012). ChIP-seq guidelines and practices of the ENCODE and modENCODE consortia. *Genome Res, 22*(9), 1813-1831. doi:10.1101/gr.136184.111

Lange, J., Yamada, S., Tischfield, S. E., Pan, J., Kim, S., Zhu, X., . . . Keeney, S. (2016). The Landscape of Mouse Meiotic Double-Strand Break Formation, Processing, and Repair. *Cell, 167*(3), 695-708 e616. doi:10.1016/j.cell.2016.09.035

Li, M., Huang, T., Li, M. J., Zhang, C. X., Yu, X. C., Yin, Y. Y., . . . Liu, K. (2019). The histone modification reader ZCWPW1 is required for meiosis prophase I in male but not in female mice. *Sci Adv, 5*(8), eaax1101. doi:10.1126/sciadv.aax1101

Lichten, M., & de Massy, B. (2011). The impressionistic landscape of meiotic recombination. *Cell, 147*(2), 267-270. doi:S0092-8674(11)01149-4 [pii]10.1016/j.cell.2011.09.038 [doi]

Litwin, I., Bakowski, T., Maciaszczyk-Dziubinska, E., & Wysocki, R. (2017). The LSH/HELLS homolog Irc5 contributes to cohesin association with chromatin in yeast. *Nucleic Acids Res, 45*(11), 6404-6416. doi:10.1093/nar/gkx240

Litwin, I., Bakowski, T., Szakal, B., Pilarczyk, E., Maciaszczyk-Dziubinska, E., Branzei, D., & Wysocki, R. (2018). Error-free DNA damage tolerance pathway is facilitated by the Irc5 translocase through cohesin. *EMBO J, 37*(18). doi:10.15252/embj.201798732

Lungu, C., Muegge, K., Jeltsch, A., & Jurkowska, R. Z. (2015). An ATPase-deficient variant of the SNF2 family member HELLS shows altered dynamics at pericentromeric heterochromatin. *J Mol Biol, 427*(10), 1903-1915. doi:10.1016/j.jmb.2015.03.014

Mahgoub, M., Paiano, J., Bruno, M., Wu, W., Pathuri, S., Zhang, X., . . . Macfarlan, T. S. (2020). Dual histone methyl reader ZCWPW1 facilitates repair of meiotic double strand breaks in male mice. *elife, 9*. doi:10.7554/eLife.53360

Mayran, A., & Drouin, J. (2018). Pioneer transcription factors shape the epigenetic landscape. *J Biol Chem, 293*(36), 13795-13804. doi:10.1074/jbc.R117.001232

Mihola, O., Pratto, F., Brick, K., Linhartova, E., Kobets, T., Flachs, P., . . . Trachtulec, Z. (2019). Histone methyltransferase PRDM9 is not essential for meiosis in male mice. *Genome Res, 29*(7), 1078-1086. doi:10.1101/gr.244426.118

Morin, R., Bainbridge, M., Fejes, A., Hirst, M., Krzywinski, M., Pugh, T., . . . Marra, M. (2008). Profiling the HeLa S3 transcriptome using randomly primed cDNA and massively parallel short-read sequencing. *Biotechniques, 45*(1), 81-94. doi:10.2144/000112900

Myant, K., & Stancheva, I. (2008). LSH cooperates with DNA methyltransferases to repress transcription. *Mol Cell Biol, 28*(1), 215-226. doi:10.1128/MCB.01073-07

Nakatani, Y., & Ogryzko, V. (2003). Immunoaffinity purification of mammalian protein complexes. *Methods Enzymol, 370*, 430-444. doi:10.1016/S0076-6879(03)70037-8

Pan, J., Sasaki, M., Kniewel, R., Murakami, H., Blitzblau, H. G., Tischfield, S. E., . . . Keeney, S. (2011). A Hierarchical Combination of Factors Shapes the Genome-wide Topography of Yeast Meiotic Recombination Initiation. *Cell, 144*(5), 719-731. doi:S0092-8674(11)00123-1 [pii]10.1016/j.cell.2011.02.009 [doi]

Papanikos, F., Clement, J. A. J., Testa, E., Ravindranathan, R., Grey, C., Dereli, I., . . . Toth, A. (2019). Mouse ANKRD31 Regulates Spatiotemporal Patterning of Meiotic Recombination Initiation and Ensures Recombination between X and Y Sex Chromosomes. *Mol Cell, 74*(5), 1069-1085 e1011. doi:10.1016/j.molcel.2019.03.022

Peters, A. H., Plug, A. W., van Vugt, M. J., & de Boer, P. (1997). A drying-down technique for the spreading of mammalian meiocytes from the male and female germline. *Chromosome Res,*

5(1), 66-68. Retrieved from http://www.ncbi.nlm.nih.gov/htbin-post/Entrez/query?db=m&form=6&dopt=r&uid=9088645

Powers, N. R., Parvanov, E. D., Baker, C. L., Walker, M., Petkov, P. M., & Paigen, K. (2016). The Meiotic Recombination Activator PRDM9 Trimethylates Both H3K36 and H3K4 at Recombination Hotspots In Vivo. *PLoS Genet, 12*(6), e1006146. doi:10.1371/journal.pgen.1006146

Pratto, F., Brick, K., Khil, P., Smagulova, F., Petukhova, G. V., & Camerini-Otero, R. D. (2014). DNA recombination. Recombination initiation maps of individual human genomes. *Science, 346*(6211), 1256442. doi:10.1126/science.1256442

Ren, J., Finney, R., Ni, K., Cam, M., & Muegge, K. (2019). The chromatin remodeling protein Lsh alters nucleosome occupancy at putative enhancers and modulates binding of lineage specific transcription factors. *Epigenetics, 14*(3), 277-293. doi:10.1080/15592294.2019.1582275

Romer, K. A., de Rooij, D. G., Kojima, M. L., & Page, D. C. (2018). Isolating mitotic and meiotic germ cells from male mice by developmental synchronization, staging, and sorting. *Dev Biol, 443*(1), 19-34. doi:10.1016/j.ydbio.2018.08.009

Sadate-Ngatchou, P. I., Payne, C. J., Dearth, A. T., & Braun, R. E. (2008). Cre recombinase activity specific to postnatal, premeiotic male germ cells in transgenic mice. *Genesis, 46*(12), 738-742. doi:10.1002/dvg.20437

Sasaki, M., Lange, J., & Keeney, S. (2010). Genome destabilization by homologous recombination in the germ line. *Nat Rev Mol Cell Biol, 11*(3), 182-195. doi:nrm2849 [pii]10.1038/nrm2849 [doi]

Schwenk, F., Baron, U., & Rajewsky, K. (1995). A cre-transgenic mouse strain for the ubiquitous deletion of loxP-flanked gene segments including deletion in germ cells. *Nucleic Acids Res, 23*(24), 5080-5081. doi:10.1093/nar/23.24.5080

Seisenberger, S., Andrews, S., Krueger, F., Arand, J., Walter, J., Santos, F., . . . Reik, W. (2012). The dynamics of genome-wide DNA methylation reprogramming in mouse primordial germ cells. *Mol Cell, 48*(6), 849-862. doi:10.1016/j.molcel.2012.11.001

Serandour, A. A., Avner, S., Oger, F., Bizot, M., Percevault, F., Lucchetti-Miganeh, C., . . . Salbert, G. (2012). Dynamic hydroxymethylation of deoxyribonucleic acid marks differentiation-associated enhancers. *Nucleic Acids Res, 40*(17), 8255-8265. doi:10.1093/nar/gks595

Smagulova, F., Brick, K., Pu, Y., Camerini-Otero, R. D., & Petukhova, G. V. (2016). The evolutionary turnover of recombination hot spots contributes to speciation in mice. *Genes Dev, 30*(3), 266-280. doi:10.1101/gad.270009.115

Smagulova, F., Gregoretti, I. V., Brick, K., Khil, P., Camerini-Otero, R. D., & Petukhova, G. V. (2011). Genome-wide analysis reveals novel molecular features of mouse recombination hotspots. *Nature, 472*(7343), 375-378. doi:nature09869 [pii]10.1038/nature09869

Spruce, C., Dlamini, S., Ananda, G., Bronkema, N., Tian, H., Paigen, K., . . . Baker, C. L. (2020). HELLS And PRDM9 form a pioneer complex to open chromatin at meiotic recombination hot spots. *Genes Dev*. doi:10.1101/gad.333542.119

Spruijt, C. G., Gnerlich, F., Smits, A. H., Pfaffeneder, T., Jansen, P. W., Bauer, C., . . . Vermeulen, M. (2013). Dynamic readers for 5-(hydroxy)methylcytosine and its oxidized derivatives. *Cell, 152*(5), 1146-1159. doi:10.1016/j.cell.2013.02.004

Strom, L., Lindroos, H. B., Shirahige, K., & Sjogren, C. (2004). Postreplicative recruitment of cohesin to double-strand breaks is required for DNA repair. *Mol Cell, 16*(6), 1003-1015. doi:10.1016/j.molcel.2004.11.026

Stroud, H., Greenberg, M. V., Feng, S., Bernatavichute, Y. V., & Jacobsen, S. E. (2013). Comprehensive analysis of silencing mutants reveals complex regulation of the Arabidopsis methylome. *Cell, 152*(1-2), 352-364. doi:10.1016/j.cell.2012.10.054

Szulwach, K. E., Li, X., Li, Y., Song, C. X., Han, J. W., Kim, S., . . . Jin, P. (2011). Integrating 5-hydroxymethylcytosine into the epigenomic landscape of human embryonic stem cells. *PLoS Genet, 7*(6), e1002154. doi:10.1371/journal.pgen.1002154

Tahiliani, M., Koh, K. P., Shen, Y., Pastor, W. A., Bandukwala, H., Brudno, Y., . . . Rao, A. (2009). Conversion of 5-methylcytosine to 5-hydroxymethylcytosine in mammalian DNA by MLL partner TET1. *Science, 324*(5929), 930-935. doi:10.1126/science.1170116

Unal, E., Arbel-Eden, A., Sattler, U., Shroff, R., Lichten, M., Haber, J. E., & Koshland, D. (2004). DNA damage response pathway uses histone modification to assemble a double-strand break-specific cohesin domain. *Mol Cell, 16*(6), 991-1002. doi:10.1016/j.molcel.2004.11.027

Van Aelst, L., Barr, M., Marcus, S., Polverino, A., & Wigler, M. (1993). Complex formation between RAS and RAF and other protein kinases. Proc Natl Acad Sci U S A, 90(13), 6213-6217. doi:10.1073/pnas.90.13.6213

Vara, C., Capilla, L., Ferretti, L., Ledda, A., Sanchez-Guillen, R. A., Gabriel, S. I., . . . Ruiz-Herrera, A. (2019). PRDM9 diversity at fine geographical scale reveals contrasting evolutionary patterns and functional constraints in natural populations of house mice. *Mol Biol Evol*. doi:10.1093/molbev/msz091

Wells, D., Bitoun, E., Moralli, D., Zhang, G., Hinch, A. G., Donnelly, P., . . . Myers, S. R. (2019). ZCWPW1 is recruited to recombination hotspots by PRDM9, and is essential for meiotic double strand break repair. *Biorxiv*.

Williams, K., Christensen, J., & Helin, K. (2011). DNA methylation: TET proteins-guardians of CpG islands? *EMBO Rep, 13*(1), 28-35. doi:10.1038/embor.2011.233

Wu, H., Mathioudakis, N., Diagouraga, B., Dong, A., Dombrovski, L., Baudat, F., . . . Kadlec, J. (2013). Molecular Basis for the Regulation of the H3K4 Methyltransferase Activity of PRDM9. *Cell Rep, 5*(1), 13-20. doi:10.1016/j.celrep.2013.08.035

Yamada, S., Hinch, A. G., Kamido, H., Zhang, Y., Edelmann, W., & Keeney, S. (2020). Molecular structures and mechanisms of DNA break processing in mouse meiosis. *Genes Dev*. doi:10.1101/gad.336032.119

Yu, W., Briones, V., Lister, R., McIntosh, C., Han, Y., Lee, E. Y., . . . Muegge, K. (2014). CG hypomethylation in Lsh-/- mouse embryonic fibroblasts is associated with de novo H3K4me1 formation and altered cellular plasticity. *Proc Natl Acad Sci U S A, 111*(16), 5890-5895. doi:10.1073/pnas.1320945111

Yu, W., McIntosh, C., Lister, R., Zhu, I., Han, Y., Ren, J., . . . Muegge, K. (2014). Genome-wide DNA methylation patterns in LSH mutant reveals de-repression of repeat elements and redundant epigenetic silencing pathways. *Genome Res, 24*(10), 1613-1623. doi:10.1101/gr.172015.114

Zeng, W., Baumann, C., Schmidtmann, A., Honaramooz, A., Tang, L., Bondareva, A., . . . Dobrinski, I. (2011). Lymphoid-specific helicase (HELLS) is essential for meiotic progression in mouse spermatocytes. *Biol Reprod, 84*(6), 1235-1241. doi:10.1095/biolreprod.110.085720

Zhu, H., Geiman, T. M., Xi, S., Jiang, Q., Schmidtmann, A., Chen, T., . . . Muegge, K. (2006). Lsh is involved in de novo methylation of DNA. *EMBO J, 25*(2), 335-345. doi:10.1038/sj.emboj.7600925

Figure legends

Figure 1. HELLS interacts with PRDM9

(A) Domains of PRDM9 and HELLS

PRDM9 includes a Krüppel-associated box domain (KRAB), a synovial sarcoma-X break point-repression domain (SSXRD), a Su(var)3-9, Polycomb-group protein enhancer of zeste and trithorax-group protein TRX domain (PR/SET) that is preceded and followed by zinc finger domains (ZK and ZF, respectively), and a C2H2-type zinc finger array (C2H2 ZF array). HELLS contains a coiled-coil domain, a helicase ATPase domain, and a helicase C-terminal domain.

(B) Interaction between PRDM9 and HELLS by yeast two-hybrid assays.

Full length and four fragments of mouse HELLS were used to test for interaction with mouse PRDM9 (full length). HELLS domains were fused to the Gal4 activation domain (GAD), and PRDM9 was fused to the Gal4 DNA binding domain (GBD). A positive interaction was detected for full length HELLS and fragment 1-569. Growth was tested on medium without leucine and tryptophan (LW), without leucine, tryptophan and histidine (LWH), and without leucine, tryptophan and histidine with 5mM amino-triazole (LWH + 5mM AT). A diploid strain that expresses pGAD-REC114 and pGBD-MEI4 (Kumar, Bourbon, & de Massy, 2010) was used as positive control. The HELLS region of the cDNAs isolated by yeast two-hybrid (Y2H) screening is shown. Controls are shown in Figure 1- figure supplement 1.

Figure 2. Meiotic prophase is defective in *Hells* cKO spermatocytes

(A) Detection of PRDM9, HELLS and SYCP3 expression in nuclear fractions of testes from *Hells* CTRL (*Hells*$^{fl/+}$ and *Hells*$^{fl/-}$) and *Hells* cKO mice at 22 dpp. *Hells* alleles are presented in Figure 2- figure supplement 1. HELLS and PRDM9 expression are presented in Figure 2-figure supplement 2.

(B) Representative spreads of early zygotene spermatocyte nuclei from synchronized testes from *Hells* CTRL and *Hells* cKO mice after staining for DNA (DAPI, white or blue), SYCP3 (white or red) and HELLS (white or green) (top panels) or PRDM9 (white or green) (bottom panels). Anti-HELLS antibody from rabbit was used for these staining. Scale bar, 10 μm. HELLS and PRDM9 detection kinetics are presented in Figure 2- figure supplement 3 and 5.

(C) Periodic acid-Schiff (PAS) staining of testis sections from 40 dpp *Hells* CTRL and *Hells* cKO mice. To visualize the glycoproteins/acrosomes (violet) and nuclei (blue), testis sections were stained with PAS and counterstained with hematoxylin. *Hells* CTRL testis sections (left panel) show normal spermatogenesis with well-organized stages of germ cell development, round spermatids with PAS-positive normal acrosomal caps, elongating and elongated spermatids. *Hells* cKO testis sections (right panel) show defective spermatogenesis with only few elongated spermatids (black arrow). Scale bar, 50μm.

(D) Proportions of seminiferous tubules without and with spermatids (mean ± SD) in testis sections from *Hells* CTRL and *Hells* cKO mice at 40 dpp. n=4 testis sections from 2 mice. Data are available in Figure 2- source data File 1.

(E) Apoptosis detected by TUNEL assay in *Hells* CTRL and *Hells* cKO testes at 40 dpp. n=2 testis sections from 1 mouse. TUNEL-positive cells are shown in Figure 2- figure supplement 4. Data are available in Figure 2- source data File 1.

(F) SYCP3 (red) and SYCP1 (green) staining of pachytene (*Hells* CTRL) and pachytene-like (*Hells* cKO) spermatocyte nuclei from 40 dpp mice. Arrowheads, unsynapsed chromosomes. White arrow, non-homologous synapsis. Blue arrows, sex chromosomes. Scale bar, 10 μm.

(G) Representative spreads of early zygotene and pachytene or pachytene-like spermatocyte nuclei from 40 dpp *Hells* CTRL and *Hells* cKO mice, respectively, after staining for SYCP3 (white or red), DMC1 (white or green) and γH2AFX (white or blue). Scale bar, 10 μm.

Figure 3. HELLS is required for the formation of meiotic DSBs at sites of PRDM9-dependent DSB formation; DSBs are directed at default sites in the absence of HELLS

(A) Limited overlapping between DSB hotspots from *Hells* CTRL and *Hells* cKO testis samples. Only hotspot centers (DMC1-SSDS peaks) that overlapped within a 400bp-window were considered as common. The others were considered as *Hells* CTRL - or *Hells* cKO-specific hotspots. Controls are shown in Figure 3- figure supplement 1.

(B) Distribution of the DMC1-SSDS signal from *Hells* CTRL and *Hells* cKO testis samples around *Hells* CTRL, *Hells* cKO and common hotspots (as defined in Figure 3A). The heatmaps show the DMC1-SSDS normalized fragments per million, calculated in a -5kb to +5kb window around hotspot centers and averaged within 10bp-bins. For the *Hells* CTRL - or *Hells* cKO-specific hotspots, the sites on the heatmaps were ranked by decreasing DMC1 intensity (from top to bottom) in the genotype where the peaks were detected. For the common hotspots, the sites were ranked by decreasing DMC1 intensity (from top to bottom) in *Hells* CTRL mice. The averaged profiles represent the mean DMC1-SSDS signal for each group. The analysis of common hotspots is shown in Figure 3- figure supplement 2.

(C) Wide overlapping of DSB hotspots from *Hells* cKO and *Prdm9* KO testis samples. Hotspot (DMC1-SSDS peaks) centers that overlapped within a 400bp-window were considered as common. The others were considered to be *Hells* cKO- or *Prdm9* KO-specific hotspots. *Prdm9* KO data were from GSE99921 (Brick et al., 2012).

(D) The DMC1-SSDS signal in *Prdm9* KO testis samples is either *Prdm9* KO-specific *(*i.e. not overlapping) or overlapping with *Hells* cKO-specific hotspots (as defined in Figure 3C). Density of hotspot number is plotted as a function of the DMC1 signal in *Prdm9* KO mice, expressed as FPMtype1 (type1-single strand DNA fragments Per Million of mapped reads, see methods and Khil et al., 2012 for details).

(E) DSB maps for *Hells* CTRL (blue) and *Hells* cKO (orange) testis samples (this study, two replicates for each genotype) and *Prdm9* KO testis samples (black, GSE99921 (Brick et al., 2012)) at a representative region of chromosome 1 (185.1Mb-185.5Mb).

(F) Enrichment of PRDM9 and H3K4me3 is reduced at hotspots in *Hells* cKO compared with *Hells* CTRL samples. PRDM9 and H3K4me3 ChIP/Input ratios were calculated at several B6 ($PRDM9^{Dom2}$)-specific hotspots (*Pbx1a*, *14a*, *A3*, *17b*), at the *Sycp1* promoter (only for

H3K4me3), and at two control regions that contain PRDM9^{Cst}-specific hotspots (*Psmb9.8* and *Hlx1.6*). All ratios were normalized to the ratios at *Hlx1.6*. At the four B6-specific hotspots, the difference between *Hells* cKO and *Hells* CTRL was statistically significant (two-tailed Mann-Whitney, p=0.0002). Data are available in Figure 3- source data File 1.

Figure 4. 5hmC is enriched at PRDM9-dependent sites and correlates with PRDM9 occupancy

(A) Average read enrichment and heatmaps showing 5hmC enrichment in the B6 (blue) and RJ2 (red) strains. Signal was calculated in a +/- 2kb window around hotspot centers (determined by DMC1-SSDS). 5hmC enrichment was calculated from pooled replicates within 50-bp bins and normalized by reads per million (RPM) and input. The sites on the heatmaps are ranked by decreasing DMC1-SSDS signal intensity from top to bottom.

(B) Read distribution from DMC1 and 5hmC ChIP-seq experiments in the B6 (blue) and RJ2 (red) strains at representative DMC1 PRDM9^{Dom2} (B6) and PRDM9^{Cst} (RJ2) specific sites on chromosome 1. Read distribution was calculated from pooled replicates within 50-bp bins and normalized by library size and input, except for the DMC1 ChIP experiments.

(C) Average read enrichment showing 5hmC enrichment (left y axis) and PRDM9 read enrichment (right y axis) in the B6 (blue) and RJ2 (red) strains centered in a +/- 2kb window around DMC1 B6 and DMC1 RJ2 sites, respectively. Read distribution was calculated from pooled replicates within 50-bp bins and normalized by library size and input.

(D) 5hmC signal at hotspots is HELLS-dependent. Average read enrichment showing 5hmC in the B6 (blue) and *Hells* cKO (orange) strains centered in a +/- 2kb window around the hotspot centers (DMC1-SSDS B6 sites). 5hmC enrichment was calculated from pooled replicates within 50-bp bins and normalized by read per million (RPM) and input.

(E) 5hmC signal at hotspots is dependent on PRDM9 methyltransferase activity. Average read enrichment showing 5hmC in the B6 (blue), RJ2 (orange) and B6-Tg(YF)(magenta) strains centered in a +/- 2kb window around the hotspot centers (DMC1-SSDS B6 and

RJ2 sites). 5hmC enrichment was calculated from pooled replicates within 50-bp bins and normalized by read per million (RPM) and input.

(F) 5hmC signal at hotspots is independent of DSB formation. Average read enrichment showing 5hmC enrichment in the B6 (blue) and *Spo11* KO (green) strain centered in a +/- 2kb window around the hotspot centers (DMC1-SSDS B6 sites). 5hmC enrichment was calculated form pooled replicates within 50-bp bins and normalized by read per million (RPM) and input. The duplicate analysis for all genotypes is shown in Figure 4-figure supplement 2.

Figure 5. 5hmC enrichment at DSB sites sorted by CpG content and model

(A) Average read enrichment and heatmaps showing 5hmC enrichment at DMC1-SSDS B6 sites.

(B) Average read enrichment and heatmaps showing 5hmC enrichment at DMC1-SSDS RJ2 sites. In both panels, the signal was calculated in the B6 (blue) and RJ2 (red) strain in a +/- 2kb window around the hotspot centers (determined by DMC1-SSDS) and sorted by CpG content with hotspots clustered in four groups: hotspots without CpGs, and three groups of similar size containing increasing numbers of CpGs (1-2, 3-5 and at least 6 CpGs). The number of sites for each group is indicated in the Methods section. For a given CpG content, the sites are ranked by decreasing DMC1-SSDS signal intensity from top to bottom. CpG content was calculated in a +/- 250bp window around the hotspot centers. The same analysis but at PRDM9 sites is shown in Figure 5-figure supplement 1C.

(C) Model for the targeting of DSB activity by PRDM9/HELLS in mouse male meiosis.

(a) A potential PRDM9 binding site is a specific DNA motif in a region of chromatin with no specific feature. For each nucleosome, only two histone tails (H3) are shown.

(b) The zinc finger domain of PRDM9 (ZnF) interacts with specific DNA motifs. PRDM9 may be interacting as a complex with HELLS before binding to its target sites as suggested by Spruce et al., 2020.

(c) HELLS promotes chromatin remodeling, enhancing accessibility of PRDM9 to its DNA motif and a stable interaction.

(d) PRDM9 methyltransferase catalyzes H3K4me3 and H3K36me3 on adjacent nucleosomes. These histone modifications may or not be symmetric (Lange et al., 2016). H3K9Ac is also known to be enriched near PRDM9 binding site at this stage (not shown).

(e) Putative methylated cytosines (5mC) near the PRDM9 binding site are converted to 5hmC, suggesting the recruitment of a TET enzyme.

(f) DSB forms at or adjacent to the PRDM9 binding site.

Table 1. HELLS is co-immunoprecipitated with PRDM9

Two independent immunoprecipitation experiments were performed using HeLa cells and mouse testis extracts.

In the first experiment, HeLa S3 cells that express N-terminally (Nter) or C- terminally (Cter) tagged human PRDM9 or without PRDM9 expression vector (no PRDM9) were used to identify proteins that interacts with PRDM9 after size selection (95-120 kD and 70-80 kD), and without size selection.

Mouse testis extracts were prepared without (rep1) or after incubation with benzonase (rep2) (in duplicate). IP were performed with an anti-PRDM9 antibody or with normal rabbit serum (mock).

For each protein (PRDM9 and HELLS), the total number of peptides, the protein rank in the whole set of proteins with at least 1 peptide, and ranked by number of peptides, and the sequence coverage are indicated; na: not applicable. For mouse testis extracts, the rank difference of the label free quantification intensity (LFQ) between IPs with anti-PRDM9 and mock are indicated. The full list of the identified peptides is in Supplementary File 1. Extracts analysis by electrophoresis are presented in Table 1-source data File 1.

1343

1344 **Table 1**

1345

IP	Total peptides PRDM9	Rank PRDM9	Sequence coverage PRDM9 (%)	Total peptides HELLS	Rank HELLS	Sequence coverage HELLS (%)
HeLa with size selection						
HeLa PRDM9 Nter 95-120 KD 70-80 KD	0 7	na 1/21	na 6.4	11 0	1/16 na	11.9 na
HeLa PRDM9 Cter 95-120 KD 70-80 KD	0 7	na 3/34	na 7.3	4 0	2/32 na	4.4 na
HeLa no PRDM9 95-120 KD 70-80 KD	0 0	na	na	0 0	na	na
HeLa without size selection						
HeLa PRDM9 Nter	38	6/447	29.4	97	1/447	48.1
HeLa PRDM9 Cter	35	4/364	33.7	44	1/364	37.6
HeLa no PRDM9	0	na	na	0	na	na
Mouse testis rep1						
IP PRDM9	24	27/571	35.1	14	75/571	24.1
mock	1	538/571	1.2	6	211/571	9.3
LFQ Rank difference		441			113	
Mouse testis rep2 (+benzonase)						
IP PRDM9	14 15	39/890 41/948	26.3	6 7	187/890 178/948	11
mock	1 0	782/890 na	1.4	5 1	323/890 506/948	7.2
LFQ Rank difference		870 688			122 468	

1346

1347

Source data files

Table 1- source data File 1. Purification of protein complexes

(A) Western blot analysis after complex purification by Flag-HA of extracts from HeLa S3 cells.

HeLa S3 cells without PRDM9 expression vector, or expressing human PRDM9 tagged with Flag-HA at the C-terminus (PRDM9-Ct) or N-terminus (PRDM9-Nt) were used. Protein fractions of the extracts before IP (S1: cytoplasmic fraction, S2: nuclear fraction as input for IPs, ppt: insoluble pellet) and after the affinity purification steps were analyzed by western blotting using an anti-PRDM9 antibody.

(B) Analysis of affinity-purified proteins after silver staining (sample without size selection).

Eluates 1, 2 and resin fractions obtained from affinity purification (HA) of extracts initially prepared from HeLa S3 cells without PRDM9 expression vector (M), or expressing human PRDM9 tagged with Flag-HA at the C-terminus (Ct) or at the N-terminus (Nt) were separated by electrophoresis and silver stained. Mixtures of Eluate 1 and 2 were used for mass spectrometry analysis.

(C) Western blot analysis of complex purification using an anti-PRDM9 antibody and mouse testes extracts (Mouse testis rep1). Protein extracts obtained during the Dignam-based purification (S1: cytoplasmic fraction, S2: nuclear fraction, S3: DNase-treated, and ppt: pellet) were loaded. Input (S2), unbound (UB), and proteins immunoprecipitated (IP) with an anti-PRDM9 antibody or normal rabbit serum (mock) were analyzed by western blotting. Detection was with an anti-PRDM9 antibody. Loading: 1% and 10% of input and IP samples, respectively.

(D) Analysis of affinity-purified proteins by silver staining (Mouse testis rep1). Input, and samples IP with an anti-PRDM9 antibody or with normal rabbit serum (mock) were loaded. Bovine serum albumin (BSA) was used as control. Proteins were separated by electrophoresis and silver stained.

(E) Western blot analysis of complex purification using an anti-PRDM9 antibody in extracts from mouse testes incubated with benzonase (Mouse testis rep 2), in duplicate (a and b).

Protein extracts obtained during the Dignam-based purification steps (S1: cytoplasmic fraction, S2: nuclear fraction, S3: DNase treated, and ppt: pellet) were loaded. Input (S2) and proteins IP with an anti-PRDM9 antibody or rabbit serum (mock) were analyzed by western blotting. Detection was with an anti-PRDM9 antibody. Loading: 1% and 10% of input and IP samples.

(F) Analysis of affinity purified proteins by silver staining (Mouse testis rep2). Input, and samples IP with an anti-PRDM9 antibody or with normal rabbit serum (mock) were loaded. BSA was used as control. Proteins were separated by electrophoresis and stained with silver.

Figure 2- source data File 1. Quantification of spermatid and TUNEL positive sections

Figure 3- source data File 1. PRDM9 and H3K4me3 ChIP-qPCR

Supplementary Files

Supplementary File 1. List of all the proteins identified by mass spectrometry after purification of protein complexes by immunoprecipitation of PRDM9

Proteins are displayed in four separate sheets:

HeLa S3 cell extracts with size selection. Six samples: two from Hela S3 cells that express N-terminally tagged (Nter1 and Nter2) PRDM9, two that express C-terminally tagged (Cter1 and Cter2) PRDM9, and two that do not express PRDM9 (no PRDM9).

HeLa S3 cell extracts without size selection. Three samples from Hela S3 cells that express N-terminally tagged (Nter) PRDM9, C-terminally tagged (Cter) PRDM9, or that do not express PRDM9 (no PRDM9).

Mouse testis rep1. Two samples from the IP with the anti-PRDM9 antibody and with rabbit serum (mock).

Mouse testis rep2. Four samples: two from the IP with the anti-PRDM9 antibody (PRDM9-1 and PRDM9-2) and two with rabbit serum (mock-1 and mock-2).

Proteins are ranked by peptide counts after the PRDM9 IP. Additional quantifications were performed in the mouse testis samples. These include MS/MS count, iBAQ, iBAQ rank difference between PRDM9 IP and mock, LFQ intensity and LFQ intensity rank difference between PRDM9 IP and mock.

Supplementary File 2. Sequences of the primers used for genotyping

Supplementary File 3. Sequences of the primers used for qPCR

Supplementary Figure legends

Figure 1- figure supplement 1

(A) Negative controls for the different mouse HELLS domains analyzed by yeast two-hybrid assays. Growth of diploid strains that express the indicated HELLS construct or the empty GBT9 vector were tested on medium without leucine and tryptophan (LW) and on medium without leucine, tryptophan and histidine with 5mM amino-triazole (LWH + 5mM AT). Positive control was a diploid strain that express pGAD-REC114 and pGBD-MEI4.

(B) Western blot analysis of the GAD-HELLS and GBD-PRDM9 fusion proteins expressed in the various diploid strains used in the yeast two-hybrid assays. Blots were probed with anti-GAD, anti-GBD, or anti-tubulin (internal control) antibodies, as indicated.

Figure 2- figure supplement 1. The *Hells* cKO allele

(A) Schematic diagram of the *Hells* alleles used in this study.

(B) Schematic diagram (top) and predicted sequence (bottom) of wild type (from WT or floxed allele) and mutant (KO) HELLS proteins.

Figure 2- figure supplement 2. PRDM9 and HELLS protein levels during the first wave of spermatogenesis in wild type mice

Testis extracts from RJ2 mice at the indicated days post-partum (dpp) and from adult were analyzed by western blotting. The same amount of extracts was loaded in parallel on two different gels. One membrane (left) was probed with anti-PRDM9 and anti-tubulin α antibodies, the other membrane (right) with an anti-HELLS antibody. The star on the right panel indicates non-specific bands.

Figure 2- figure supplement 3. HELLS detection in *Hells* CTRL and *Hells* cKO spermatocytes

Representative spreads of spermatocyte nuclei from *Hells* CTRL (**A**) and *Hells* cKO (**B**) mice after staining for DNA (DAPI, white), SYCP3(white or blue), and HELLS using a rabbit (white or green) and a mouse (white or red) antibody. Scale bar, 10 μm. Both rabbit and mouse anti-HELLS antibodies display a nucleus-wide, punctate staining in leptotene and zygotene stages, attributable to HELLS. In addition to this specific signal, both antibodies showed also a different non-specific signal. The mouse antibody showed a colocalization with SYCP3 at every stage, that was not seen with the rabbit antibody and is therefore most likely not attributable to HELLS. The rabbit antibody showed a nucleus-wide staining in late pachytene and diplotene stage nuclei, not seen with the mouse antibody, likely due to cross-reaction.

Figure 2- figure supplement 4. TUNEL-positive cells detected in testis sections of control and *Hells* cKO mice

Sections from 40dpp *Hells* CTRL and *Hells* cKO mice were stained for DNA (DAPI, purple) and TUNEL (green). Asterisks mark tubules containing round spermatids. Scale bar, 10 μm.

Figure 2- figure supplement 5. HELLS and PRDM9 detection in *Hells* CTRL and *Hells* cKO spermatocytes

Representative spreads of spermatocyte nuclei from *Hells* CTRL (**A**) and *Hells* cKO (**B**) mice after staining for DNA (DAPI, white), SYCP3 (white or blue), PRDM9 (white or green) and HELLS (white or red). Scale bar, 10 μm. In addition to *bona fides* HELLS staining, the mouse anti-HELLS antibody displays additional, non-specific staining marking the chromosome axes, as described in the legend to Figure 2- figure supplement 3.

Figure 3- figure supplement 1. DMC1 ChIP-SSDS reproducibility and controls

(A) The DSB map obtained using *Hells* CTRL testis samples reproduces the DSB map obtained using B6 testis samples. Hotspot (DMC1 ChIP-SSDS peaks) centers that overlapped within a 400bp-window were considered as common. The others were unique to *Hells* CTRL or B6.

(B) Comparison of the DMC1 ChIP-SSDS signal distribution in *Hells* CTRL replicates.

(C) Comparison of the DMC1 ChIP-SSDS signal distribution in *Hells* cKO replicates.

(**B-C**) The red dotted line represents the x=y. The gray scale represents the density calculated with the density2d function from R. The correlation coefficient r is indicated with the significance level (p).

Figure 3- figure supplement 2. Common hotspots between *Hells* CTRL and *Hells* cKO testis samples

(A) Comparison of the DMC1 ChIP-SSDS signals in *Hells* CTRL and *Hells* cKO samples at the common hotspots (n=1129), defined in Figure 3A. Three groups were identified: i) hotspots in which the signal was stronger in *Hells* CTRL than in *Hells* cKO (log2(*Hells* CTRL/*Hells* cKO)>1) (blue dots) (n=898 peaks); ii) hotspots in which the signal was stronger in *Hells* cKO than in *Hells* CTRL (log2(*Hells* CTRL/*Hells* cKO)<-1) (green dots) (n=154 peaks); and iii)

hotspots with comparable signal intensity in both genotypes (-1 <log2(*Hells* CTRL/*Hells* cKO)<1) (black dots) (n=77 peaks). The black dotted line represents x=y.

(B) H3K4me3 signal distribution in testis samples from the B6 (blue) and RJ2 (red) strains (GSE93955, (Grey et al., 2017)) around the three categories of common hotspots, as defined in (**A**). B6 carries a *Dom2* allele of *Prdm9* (like *Hells* CTRL and *Hells* cKO), whereas RJ2 carries the *Cast* allele. The heatmaps show a PRDM9-dependent H3K4me3 signal at the common hotspots with stronger signal in *Hells* CTRL (blue group from (**A**)), but not at the others.

Figure 4- figure supplement 1. Similar distributions of 5hmC and PRDM9 enrichments

(A) Average read enrichment and heatmaps showing 5hmC enrichment in B6 (blue) and RJ2 (red) strains centred in a +/- 2kb window around the PRDM9 B6 and RJ2 sites, respectively. 5hmC enrichment was calculated from pooled replicates within 50-bp bins and normalized by read per million and input. The sites on the heatmaps are ranked by decreasing PRDM9 signal intensity from top to bottom.

(B) Average read enrichment showing 5hmC enrichment (left y axis) and H3K4me3 or DMC1 read enrichment (right y axis) in the B6 (blue) and RJ2 (red) strains centered in a +/- 2kb window around the DMC1 B6 and DMC1 RJ2 sites, respectively. Read distribution was calculated from pooled replicates within 50-bp bins, and normalized by library size and input, except for the DMC1 ChIP experiments.

(C) Top panels: Scatter plots of 5hmC enrichment *versus* PRDM9 and H3K4me3 enrichment in the B6 (blue) and RJ2 (red) strain at the DMC1 B6 and DMC1 RJ2 sites, respectively (only sites featuring the strongest 5hmC signals, containing at least 6 CpGs in a window within +/- 250bp around hotspots were considered, see Figure 5 and Methods). Read enrichment was calculated in a window within +/-250bp around hotspots (DMC1-SSDS) normalized by library size and input. Bottom panels: Scatter plot of 5hmC read enrichment versus SPO11-oligos

peak strength (data available only for B6; (Lange et al., 2016)) and DMC1 peak strength. Rho is the Spearman correlation coefficient.

Figure 4- figure supplement 2. Reproducibility of 5hmC enrichment

Reproducibility of 5hmC enrichment in B6, RJ2, *Hells* cKO, B6-Tg(YF), and *Spo11* KO samples. Scatter plots of 5hmC read enrichment (RPM) in replicate 1 *versus* replicate 2. Blue: B6, Red: RJ2, Orange: *Hells* cKO, Purple: B6-Tg(YF), Green: *Spo11* KO. Read enrichment was calculated in a +/- 250bp window around the center of DMC1 sites normalized by library size and input. 5hmC enrichment was calculated at DMC1 B6 sites for the B6, *Hells* cKO and *Spo11* KO strains, and at DMC1 RJ2 sites for the RJ2 strain.

Figure 5- figure supplement 1.

(A) Average plot of CpG content in 100bp bins centered in a +/- 2kb window around the DMC1 B6 and DMC1 RJ2 sites.

(B) Boxplot of cytosine methylation level in the B6 mouse strain at different genomic sites. Boxes show the interquartile range (IQR; the middle 50% of scores) extending from the lower quartile (Q1; 25% of scores fall below this value) to the upper quartile (Q3; 25% of scores fall above this value). Black horizontal lines within boxes show median values. Upper and lower whiskers represent scores outside of IQR. Maximum and minimum scores show highest or lowest scores excluding outliers. DSB sites (B6 ($PRDM9^{Dom2}$): blue, and RJ ($PRDM9^{Cast}$): red), LINE (dark grey), IAP (grey), male imprinted control regions (light blue), female imprinted control regions (pink). Genome average (white). Only regions containing at least one CpG and one informative read were considered.

(C) Average read enrichment and heatmaps showing 5hmC enrichment in the B6 (blue) and RJ2 (red) strains centered in a +/- 2kb window around the PRDM9 B6 and RJ2 sites sorted by CpG content. CpG content was calculated within a window of +/- 250bp from the center of the

PRDM9 sites. For a given CpG content, the sites on the heatmaps are ranked by decreasing PRDM9 signal intensity from top to bottom.

(D) Average plots and heat maps of 5hmC, PRDM9, H3K4me3, H3K36me3 and DMC1 centered in a +/- 2kb window around DMC1 B6 sites, sorted by CpG content. For a given CpG content, the sites on the heatmaps are ranked by decreasing PRDM9, H3K4me3, H3K36me3 and DMC1 signal intensity, from top to bottom.

Figure 1

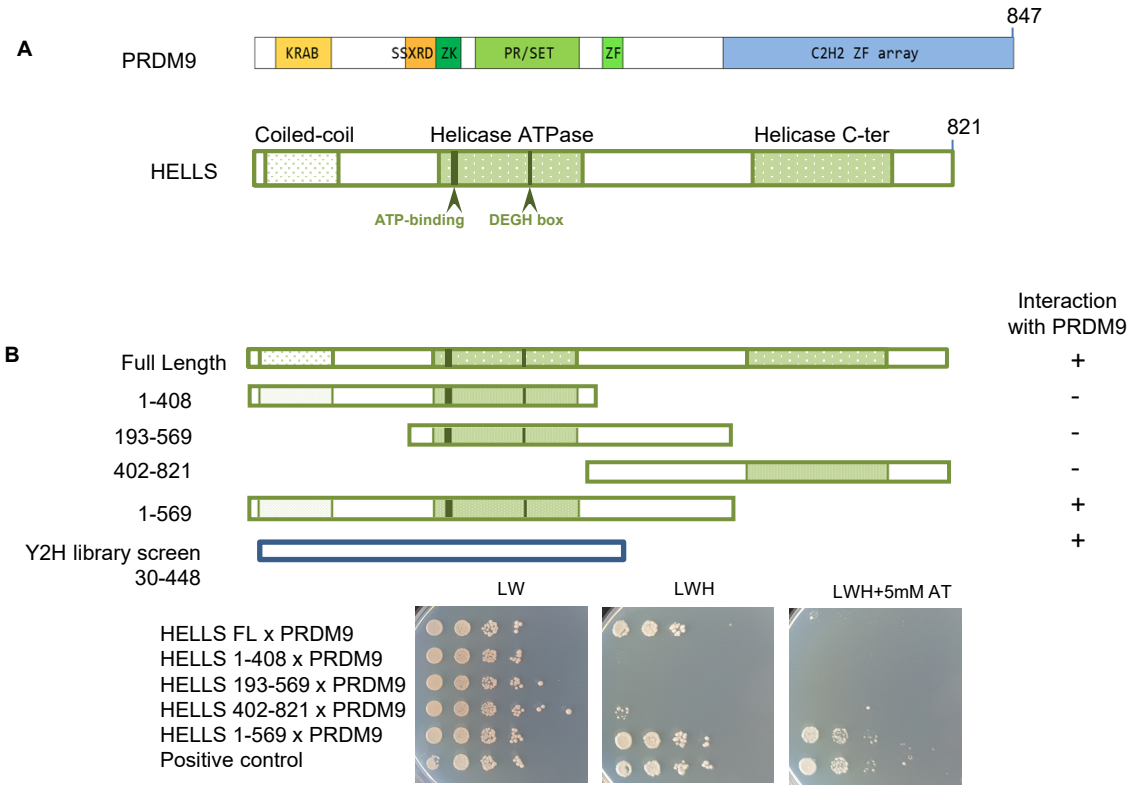
A
PRDM9
KRAB
SSXRD
ZK
PR/SET
ZF
C2H2 ZF array
847
HELLS
Coiled-coil
Helicase ATPase
Helicase C-ter
821
ATP-binding
DEGH box
B
Interaction with PRDM9
Full Length
+
1-408
-
193-569
-
402-821
-
1-569
+
Y2H library screen 30-448
+
LW
LWH
LWH+5mM AT
HELLS FL x PRDM9
HELLS 1-408 x PRDM9
HELLS 193-569 x PRDM9
HELLS 402-821 x PRDM9
HELLS 1-569 x PRDM9
Positive control

Figure 2

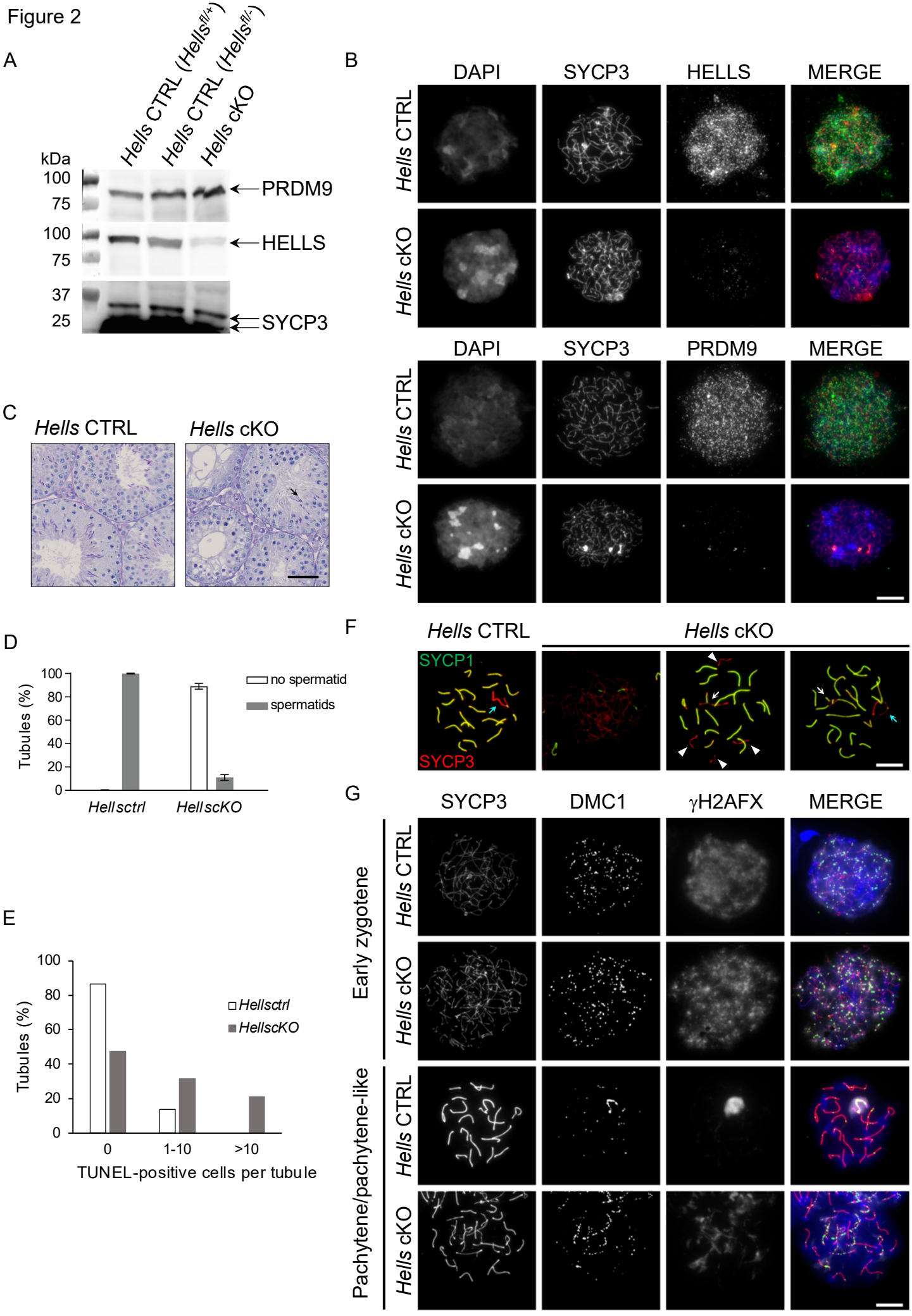
A
Hells CTRL (Hells^fl/+)
Hells CTRL (Hells^fl/-)
Hells cKO
kDa
100
75
100
75
37
25
PRDM9
HELLS
SYCP3
B
DAPI
SYCP3
HELLS
MERGE
Hells CTRL
Hells cKO
DAPI
SYCP3
PRDM9
MERGE
Hells CTRL
Hells cKO
C
Hells CTRL
Hells cKO
D
Tubules (%)
100
80
60
40
20
0
no spermatid
spermatids
Hellsctrl
HellscKO
E
Tubules (%)
100
80
60
40
20
0
Hellsctrl
HellscKO
0
1-10
>10
TUNEL-positive cells per tubule
F
Hells CTRL
Hells cKO
SYCP1
SYCP3
G
SYCP3
DMC1
γH2AFX
MERGE
Early zygotene
Hells CTRL
Hells cKO
Pachytene/pachytene-like
Hells CTRL
Hells cKO

Figure 3

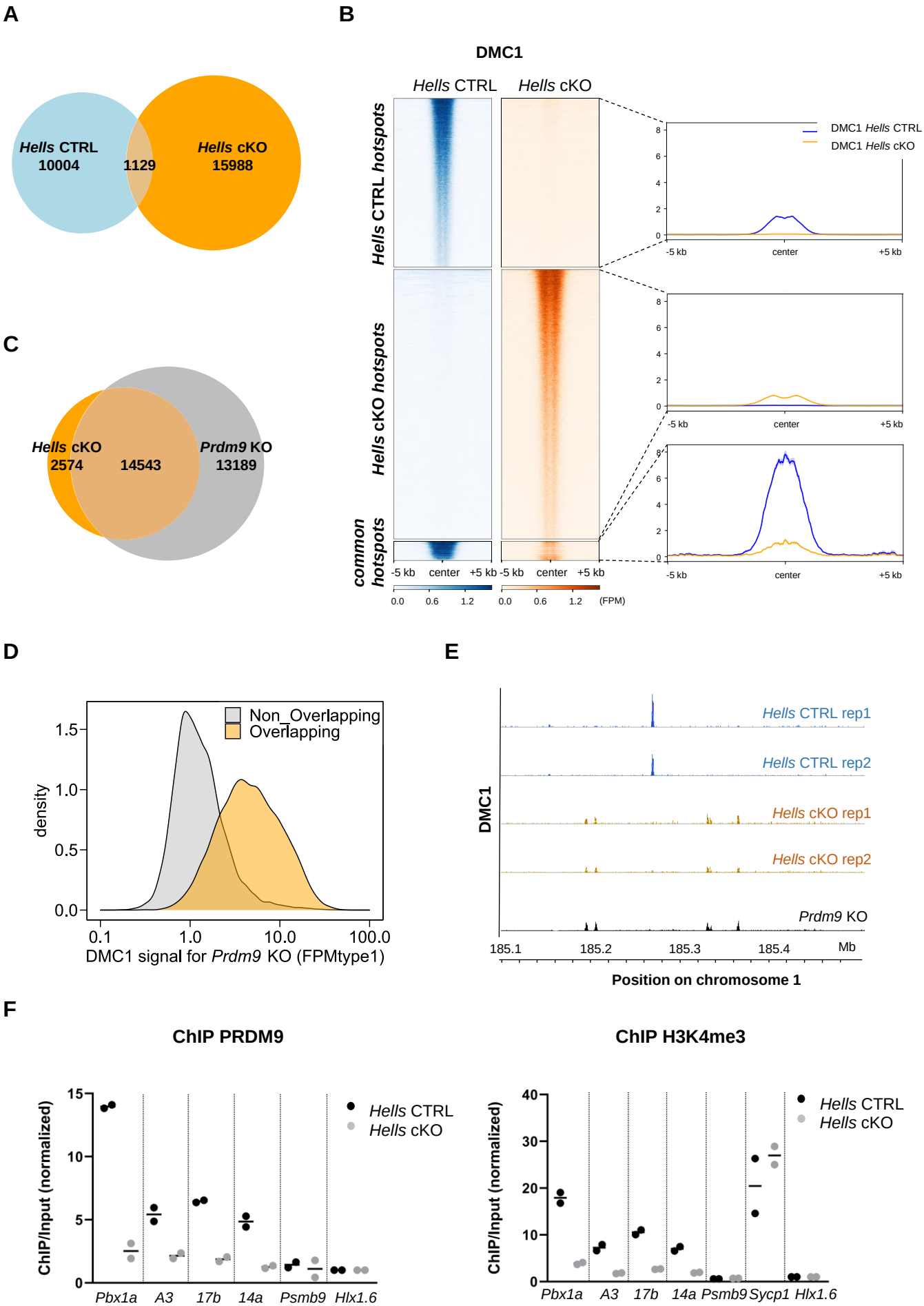
A
Hells CTRL
10004
1129
Hells cKO
15988
B
DMC1
Hells CTRL
Hells cKO
Hells CTRL hotspots
Hells cKO hotspots
common hotspots
DMC1 Hells CTRL
DMC1 Hells cKO
-5 kb
center
+5 kb
0.0
0.6
1.2
(FPM)
C
Hells cKO
2574
14543
Prdm9 KO
13189
D
Non_Overlapping
Overlapping
density
DMC1 signal for Prdm9 KO (FPMtype1)
E
DMC1
Hells CTRL rep1
Hells CTRL rep2
Hells cKO rep1
Hells cKO rep2
Prdm9 KO
185.1
185.2
185.3
185.4
Mb
Position on chromosome 1
F
ChIP PRDM9
ChIP H3K4me3
ChIP/Input (normalized)
Hells CTRL
Hells cKO
Pbx1a
A3
17b
14a
Psmb9
Sycp1
Hlx1.6

Figure 4

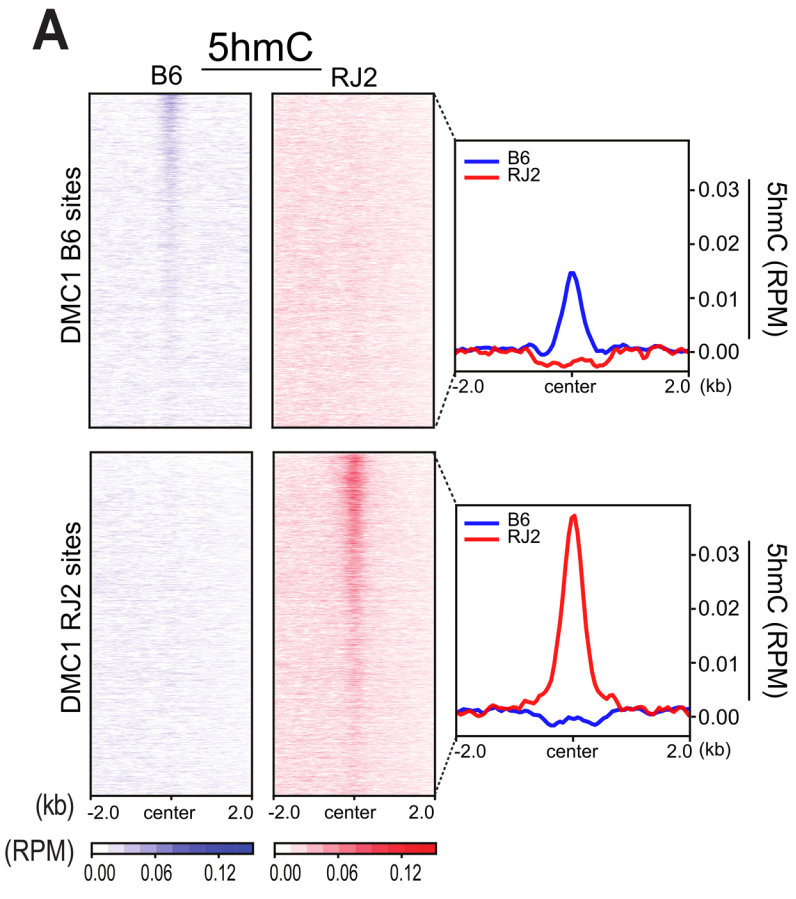
A
5hmC
B6
RJ2
DMC1 B6 sites
DMC1 RJ2 sites
B6
RJ2
5hmC (RPM)
0.03
0.02
0.01
0.00
-2.0
center
2.0 (kb)
(kb)
(RPM)
0.00 0.06 0.12

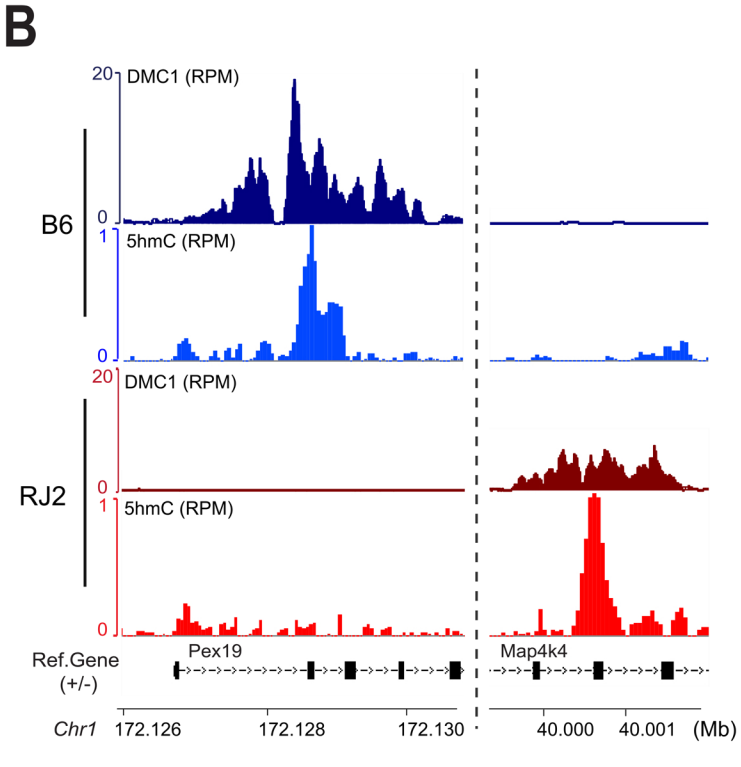
B
DMC1 (RPM)
B6
5hmC (RPM)
RJ2
Ref.Gene
(+/-)
Pex19
Map4k4
Chr1
172.126
172.128
172.130
40.000
40.001
(Mb)

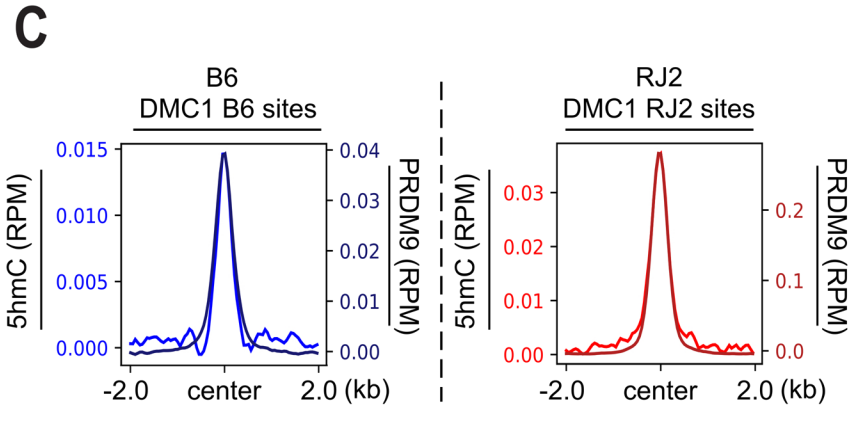
C
B6
DMC1 B6 sites
RJ2
DMC1 RJ2 sites
5hmC (RPM)
PRDM9 (RPM)
-2.0
center
2.0 (kb)

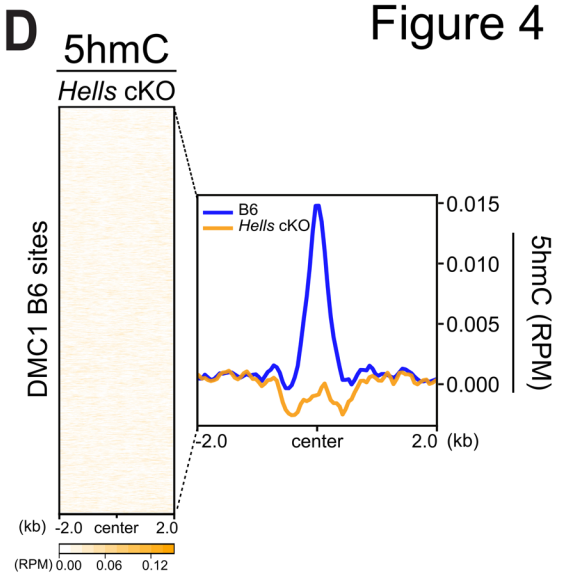
D
5hmC
Hells cKO
DMC1 B6 sites
B6
Hells cKO
5hmC (RPM)
-2.0
center
2.0 (kb)
(RPM) 0.00 0.06 0.12

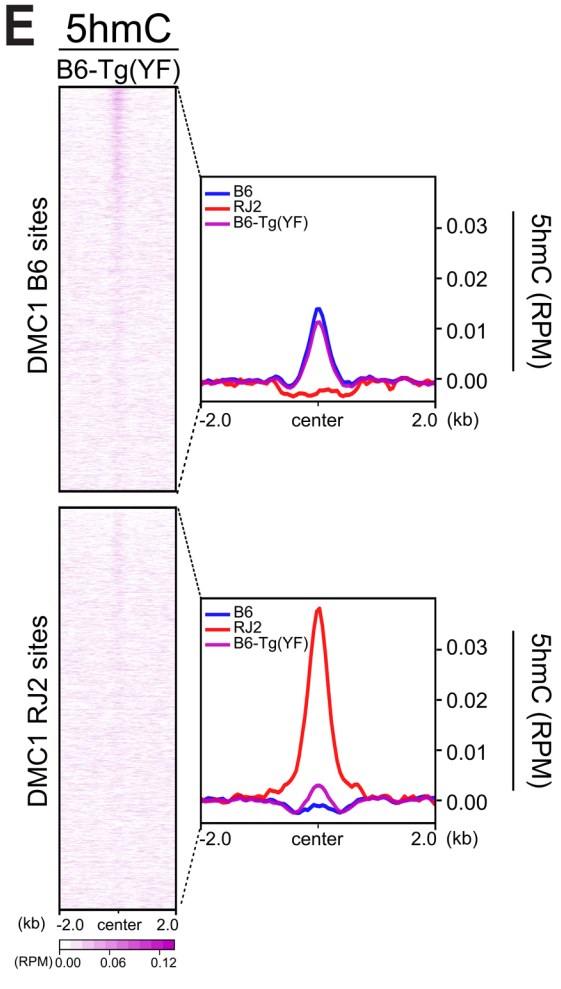
E
5hmC
B6-Tg(YF)
DMC1 B6 sites
DMC1 RJ2 sites
B6
RJ2
B6-Tg(YF)
5hmC (RPM)
-2.0
center
2.0 (kb)
(RPM) 0.00 0.06 0.12

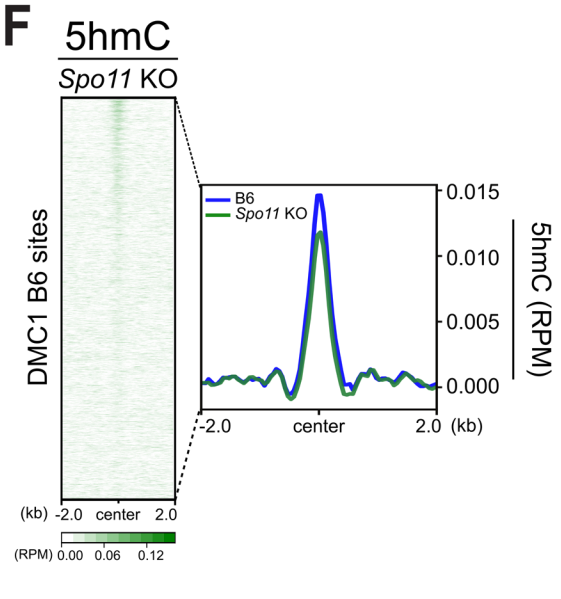
F
5hmC
Spo11 KO
DMC1 B6 sites
B6
Spo11 KO
5hmC (RPM)
-2.0
center
2.0 (kb)
(RPM) 0.00 0.06 0.12

Figure 5

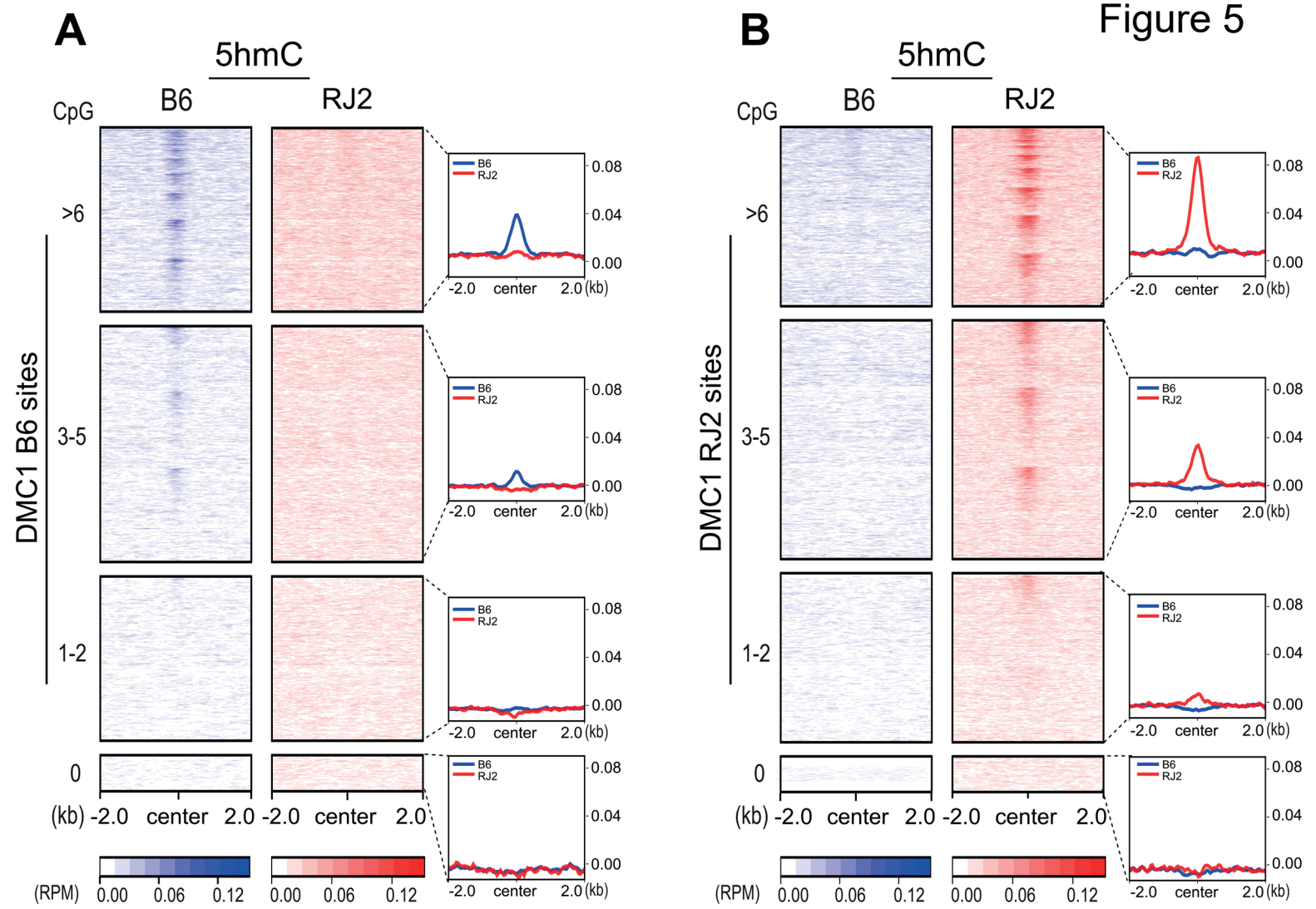

C

PRDM9 ZnF-DNA interaction

HELLS chromatin remodelling

PRDM9 stable DNA binding and histone modification

Conversion of 5mC to 5hmC

DSB formation

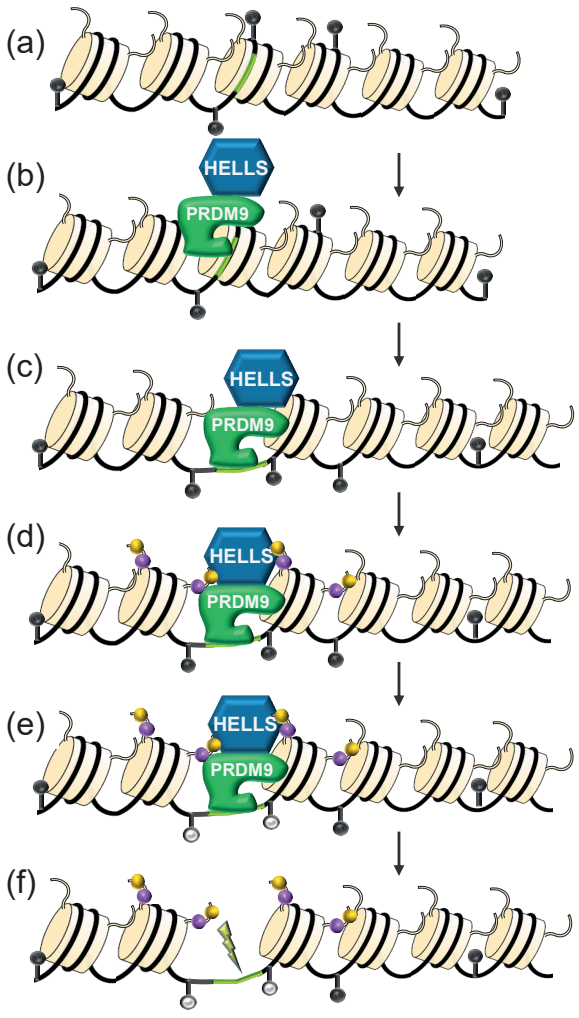

Figure 1- figure supplement 1

A

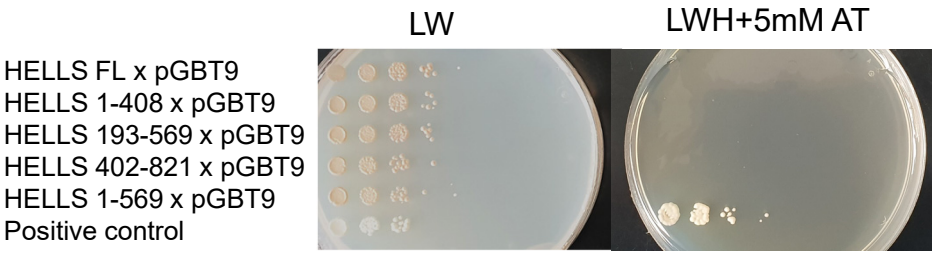

B

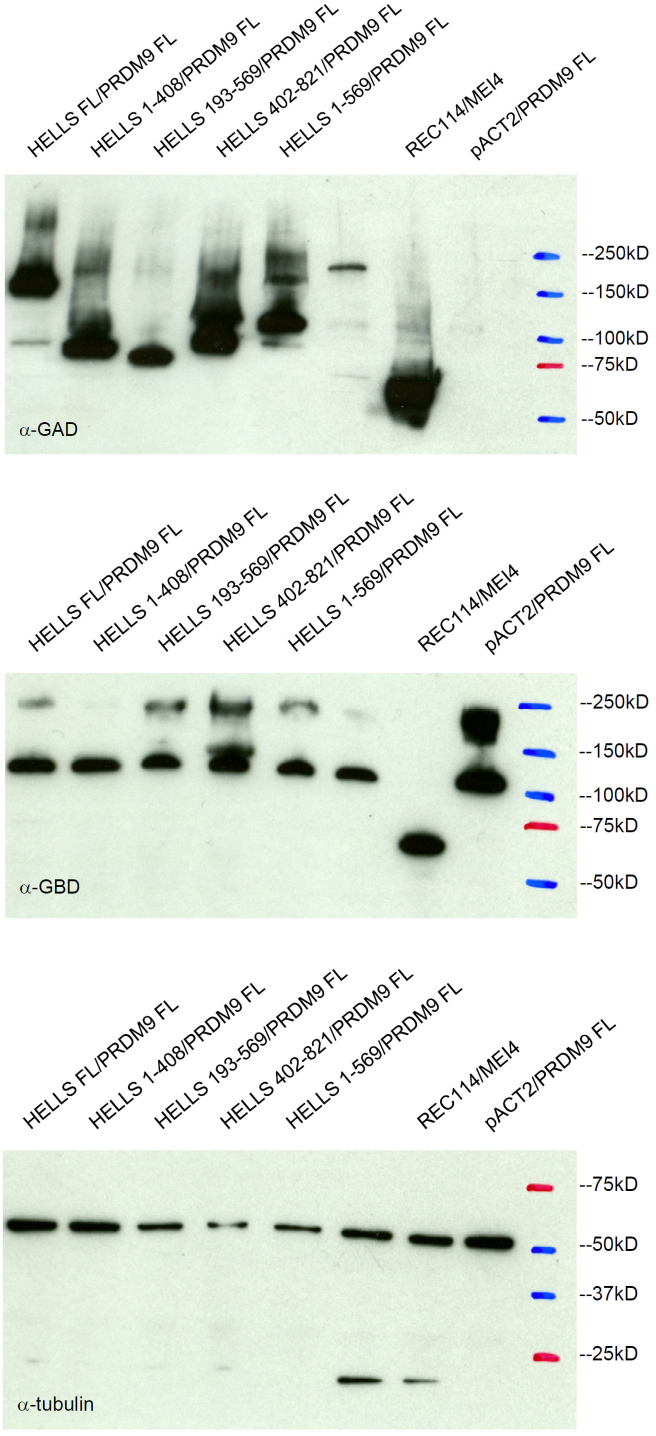

Figure 2- Figure supplement 1

A

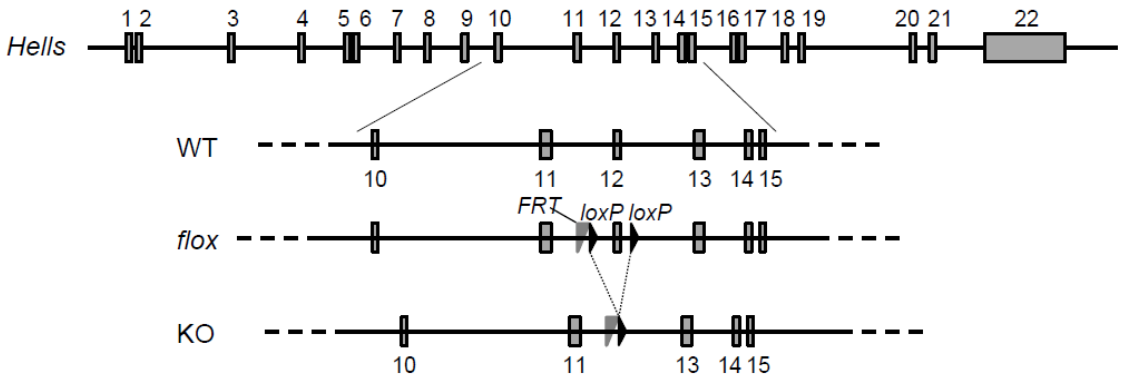

B

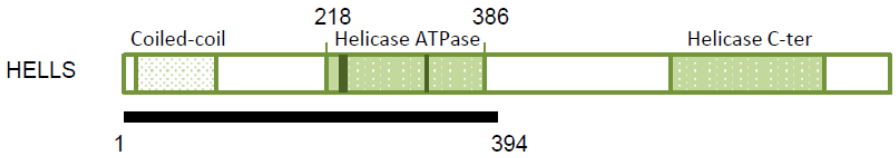


```
WT/KO   MAEQTEPAVITPAMLEEEEQLEAAGLEKERKMLEEAQKSWDRESTEIRYRRLQHLLEKSNIYSKFLLTKMEQQQLEEQKKKEKLEKKKRSLKLTEGKSLV  100
WT/KO   DGNGEKPVMKKKRGREDESYNISEVMSKEEILSVAKKHKDNEDESSSTTSLCVEDIQKNKDSNSMIKDRLSQTVRQNSKFFFDPVRKCNGQPVPFQQPKH  200
WT/KO   FTGGVMRWYQVEGMEWLRMLWENGINGILADEMGLGKTVQCIATIALMIQRGVPGPFLVCGPLSTLPNWMAEFKRFTPEIPTLLYHGTREDRRKLVKNIH  300

WT      KRQGTLQIHPVVVTSFEIAMRDQNALQHCYWKYLIVDEGHRIKNMKCRLIRELKRFNADNKLLLTGTPLQNNLSELWSLLNFLLPDVFDDLKSFESWFDI  400
        ||||||||||||||||||||||||||||||||||||||||||||||||||||||||||||||||||||||||||||||||||||||||||||||||||||||
KO      KRQGTLQIHPVVVTSFEIAMRDQNALQHCYWKYLIVDEGHRIKNMKCRLIRELKRFNADNKLLLTGTPLQNNLSELWSLLNFLLPDVFDDLKRF-  394

WT      TSLSETAEDIIAKEREQNVLHMLHQILTPFLLRRLKSDVALEVPPKREVVVYAPLCNKQEIFYTAIVNRTIANMFGSCEKETVELSPTGRPKRRSRKSIN  500
WT      YSELDQFPSELEKLISQIQPEVNRERTVVEGNIPIESEVNLKLRNIMMLLRKCCNHPYMIEYPIDPVTQEFKIDEELVTNSGKFLILDRMLPELKKRGHK  600
WT      VLVFSQMTSMLDILMDYCHLRNFIFSRLDGSMSYSEREKNIYSFNTDPDVFLFLVSTRAGGLGINLTAADTVIIYDSDWNPQSDLQAQDRCHRIGQTKPV  700
WT      VVYRLVTANTIDQKIVERAAAKRKLEKLIIHKNHFKGGQSGLSQSKNFLDAKELMELLKSRDYEREVKGSREKVISDEDLELLLDRSDLIDQMKASRPIK  800
WT      GKTGIFKILENSEDSSAECLF-  821
```

Figure 2 – figure supplement 2

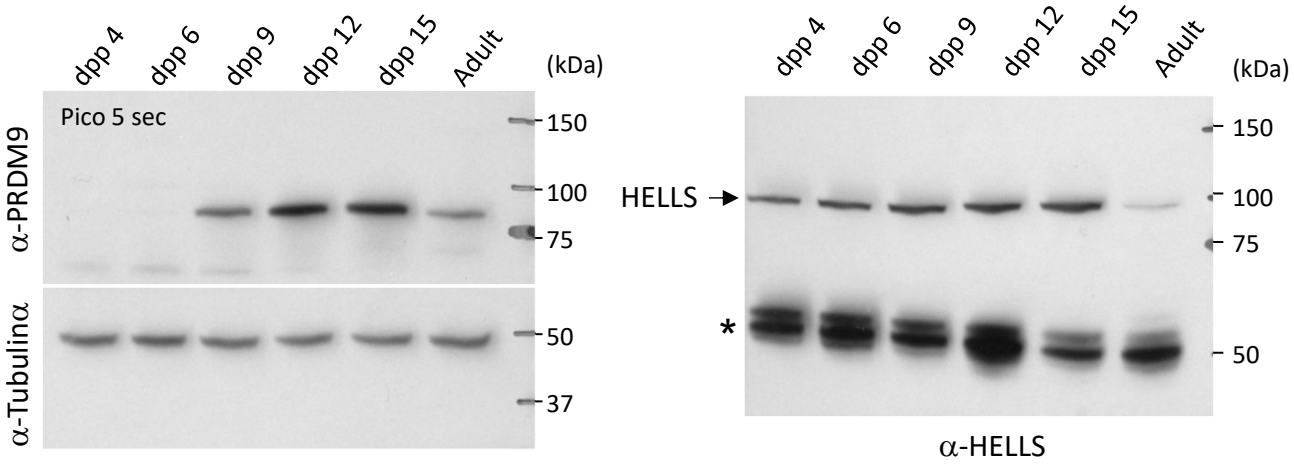

Figure 2- figure supplement 3

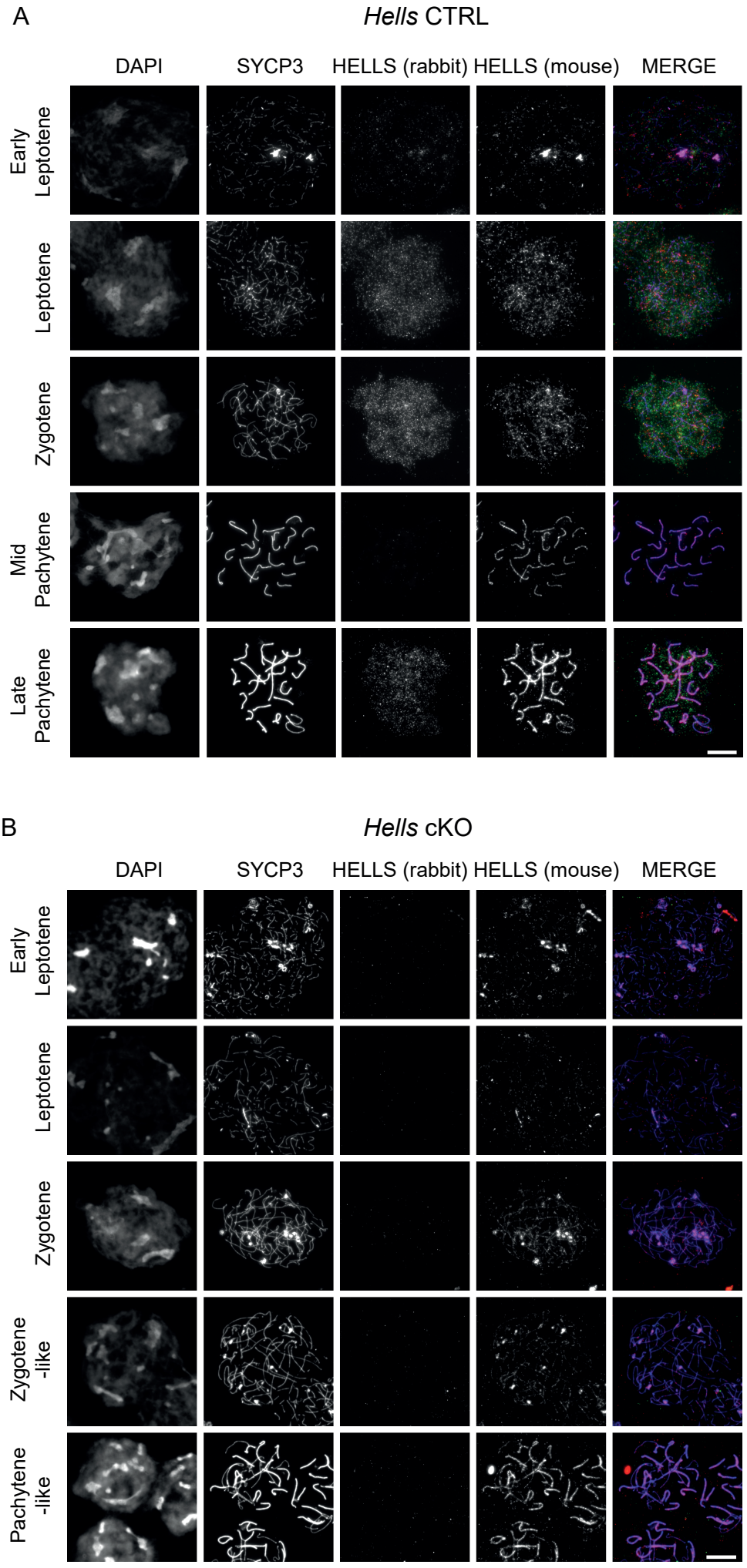

Figure 2- figure supplement 4

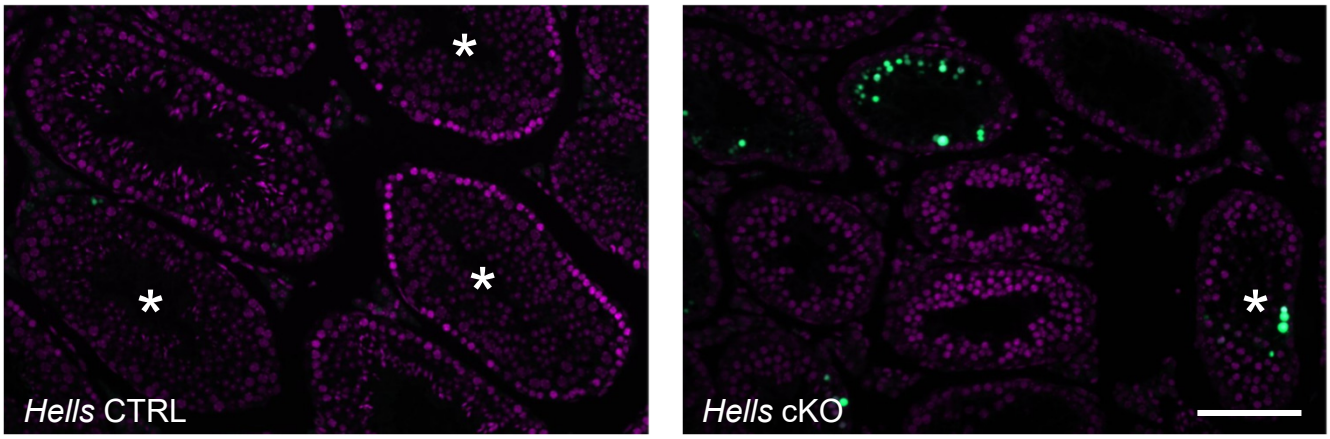

Figure 2- figure supplement 5

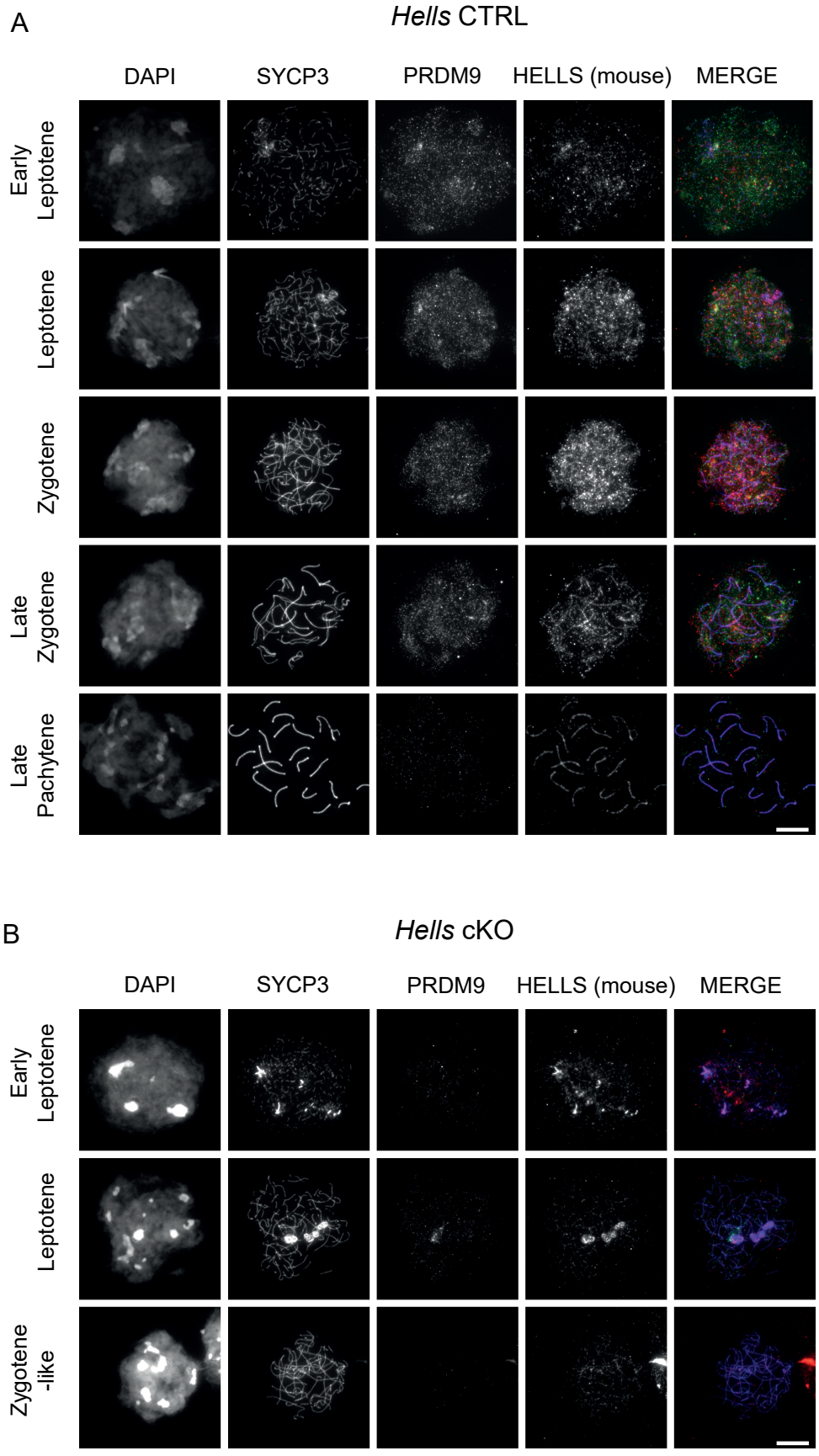

Figure 3- figure supplement 1

A

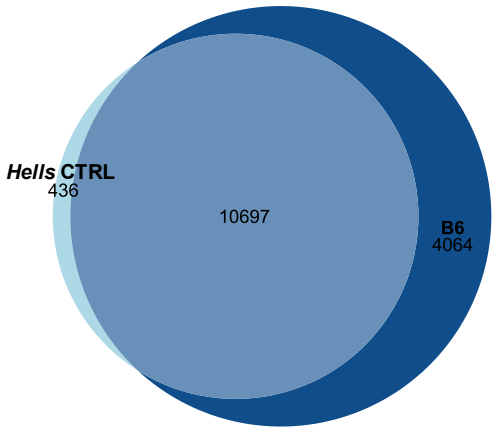

B

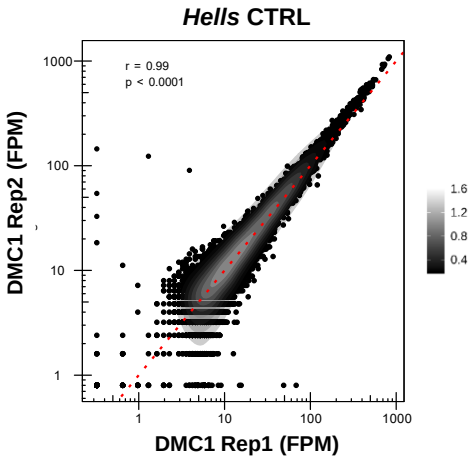

C

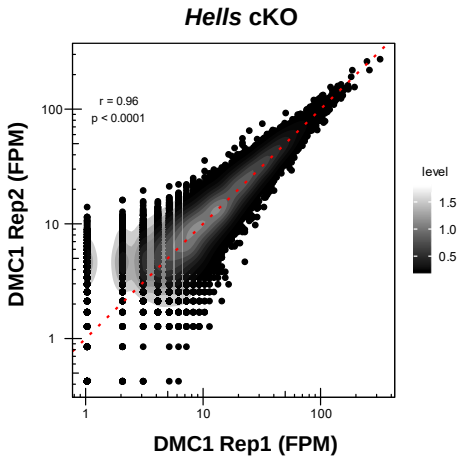

Figure 3- figure supplement 2

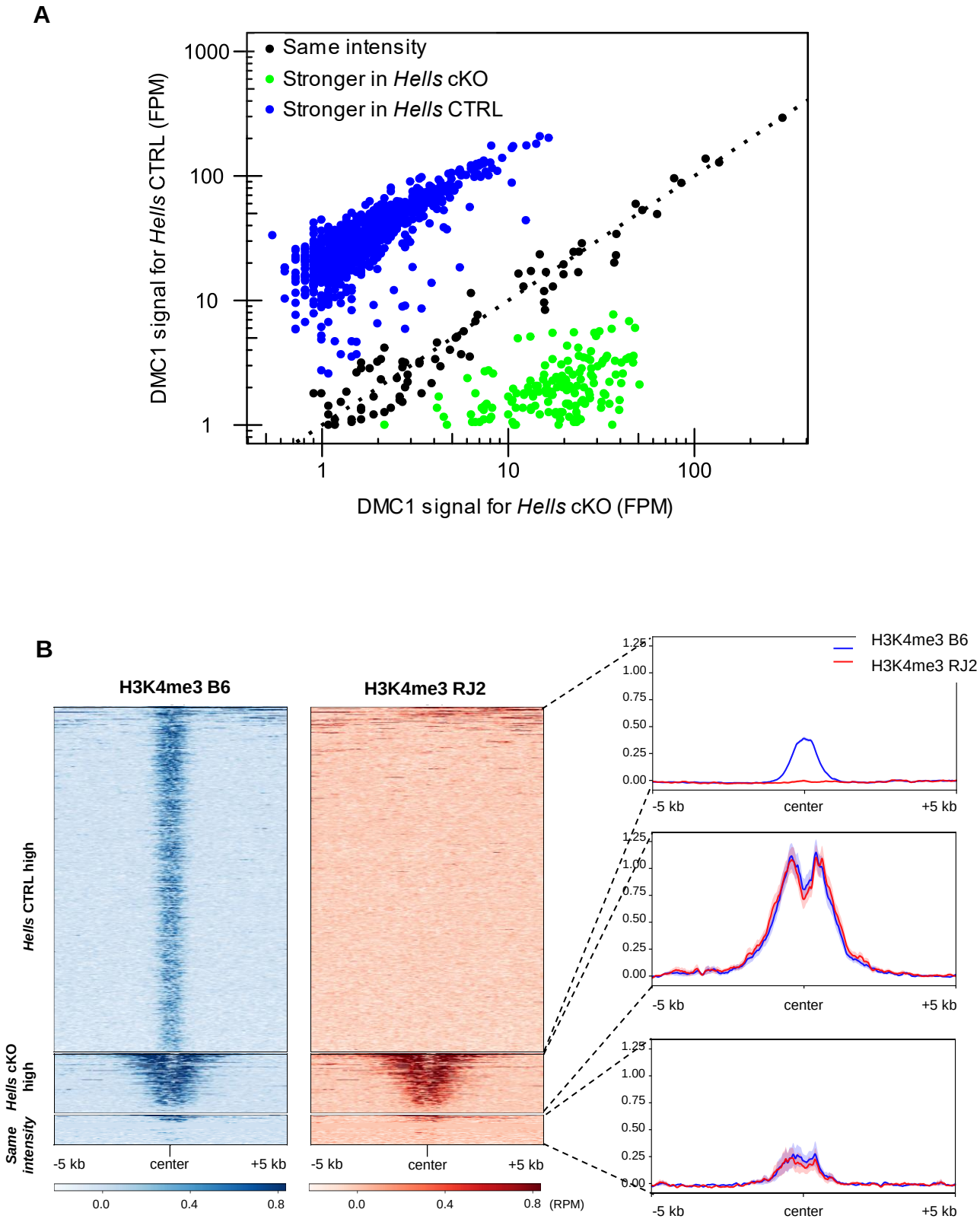

Figure 4- figure supplement 1

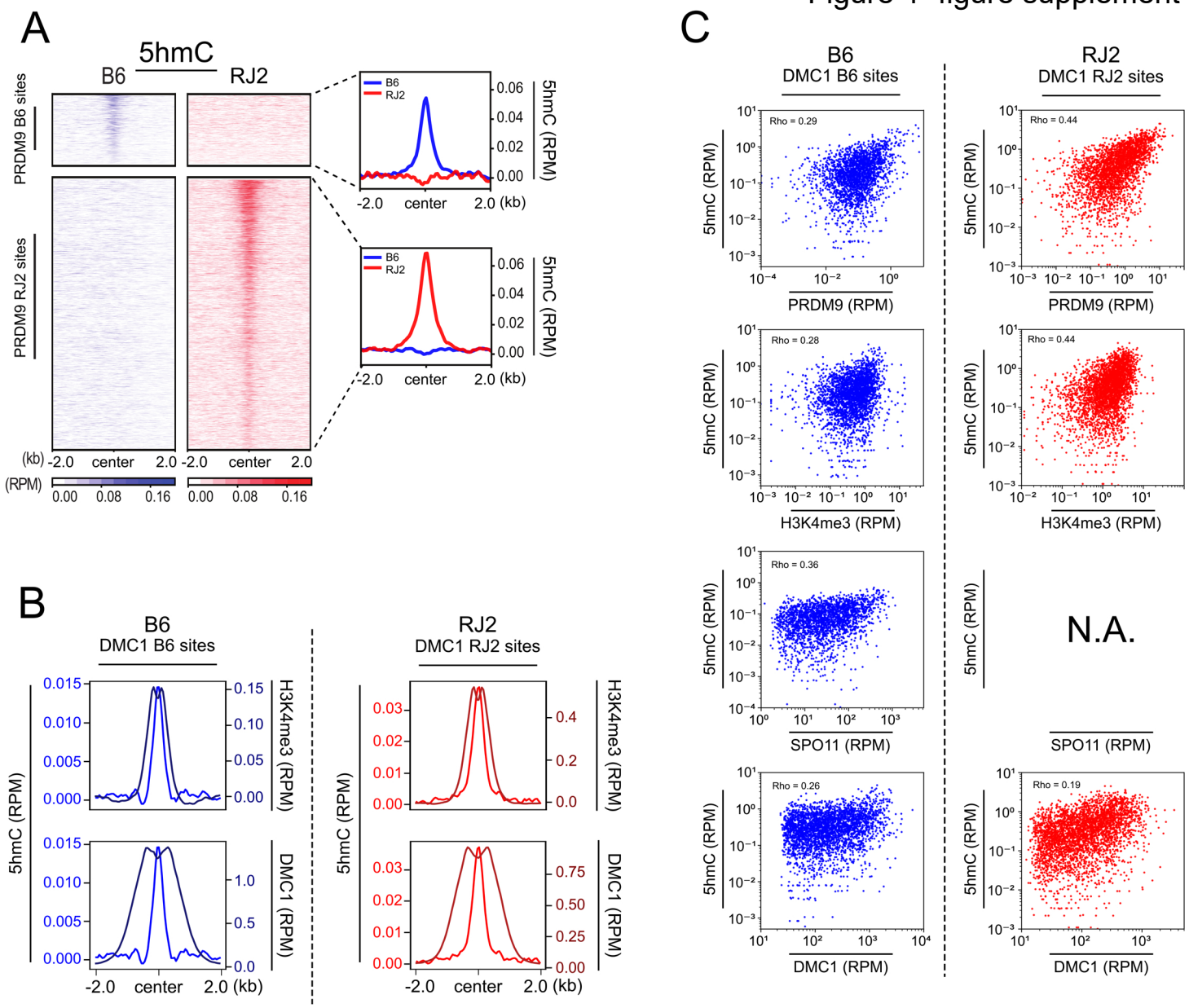

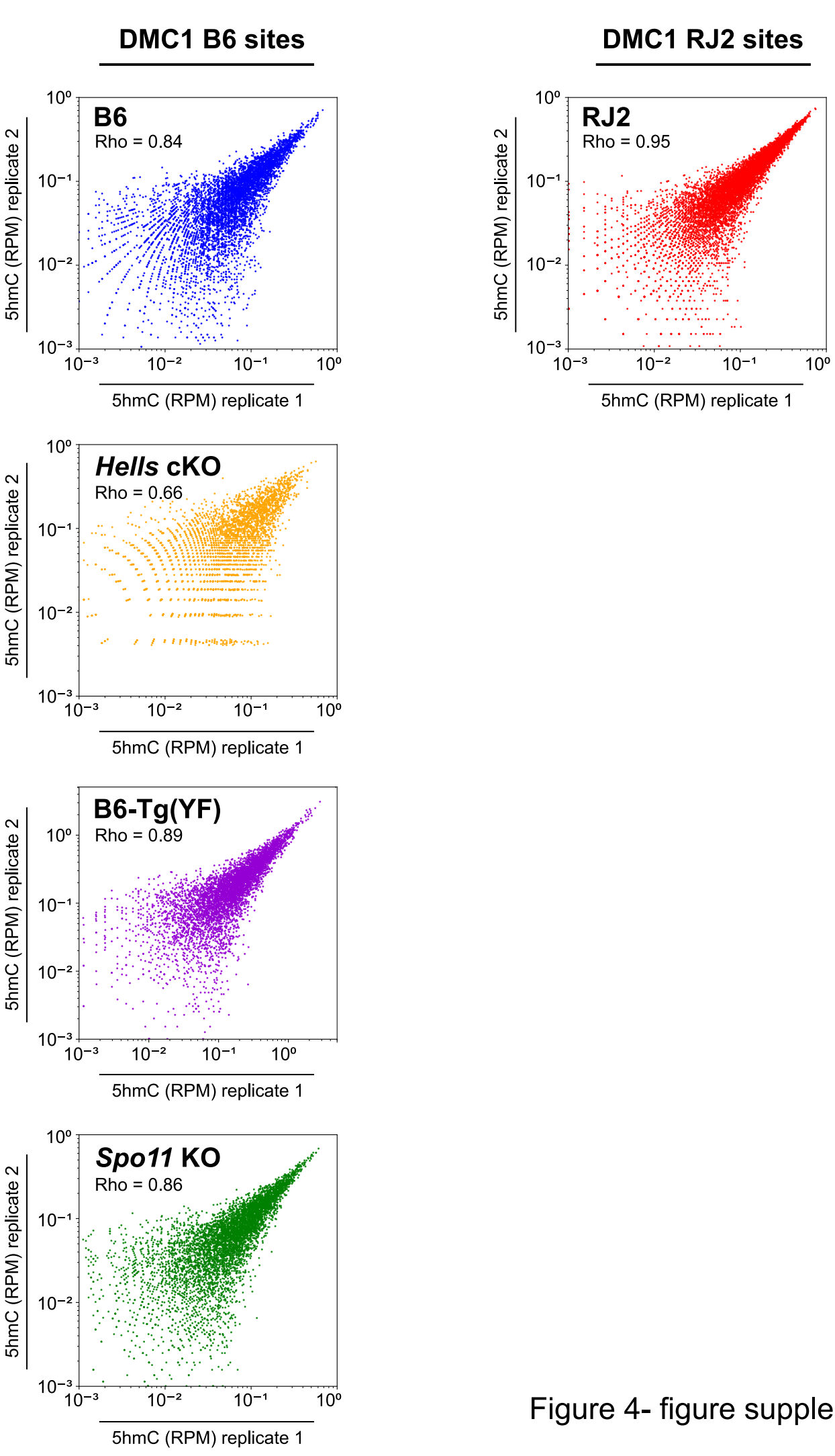

Figure 4- figure supplement 2

Figure 5- figure supplement 1